



OPEN ACCESS

EDITED BY

Ramanathan Alagappan,
Jawaharlal Nehru University, India

REVIEWED BY

Ruyue Wang,
State Key Laboratory of Shale Oil and Gas
Enrichment Mechanisms and Efficient
Development, China
Hongjian Zhu,
Yanshan University, China

*CORRESPONDENCE

Yi Shu,
✉ cugsy@sina.com
Qiming Wang,
✉ wqmpetrophysics@sina.com

RECEIVED 09 March 2025

ACCEPTED 05 June 2025

PUBLISHED 16 July 2025

CITATION

Bao H, Shu Y, Wang Q, Zheng Y, Chen M, Lu Y,
Liu H and Peng W (2025) The origin and
depositional processes of shell layers in the
Jurassic Ziliujing Formation in the Sichuan
Basin and their influences on petroleum
accumulation.
Front. Earth Sci. 13:1590482.
doi: 10.3389/feart.2025.1590482

COPYRIGHT

© 2025 Bao, Shu, Wang, Zheng, Chen, Lu, Liu
and Peng. This is an open-access article
distributed under the terms of the [Creative
Commons Attribution License \(CC BY\)](#). The
use, distribution or reproduction in other
forums is permitted, provided the original
author(s) and the copyright owner(s) are
credited and that the original publication in
this journal is cited, in accordance with
accepted academic practice. No use,
distribution or reproduction is permitted
which does not comply with these terms.

The origin and depositional processes of shell layers in the Jurassic Ziliujing Formation in the Sichuan Basin and their influences on petroleum accumulation

Hanyong Bao¹, Yi Shu^{1*}, Qiming Wang^{2*}, Youheng Zheng¹,
Miankun Chen¹, Yongchao Lu³, Haotian Liu¹ and Wei Peng¹

¹Research Institute of Exploration and Development, Jiangnan Oilfield Branch Company, Sinopec, Wuhan, China, ²School of Geosciences, China University of Petroleum (East China), Qingdao, China, ³Key Laboratory of Tectonics and Petroleum Resources of Ministry of Education, China University of Geosciences, Wuhan, China

Unlike other lacustrine shale formations in which carbonate and siliceous interlayers are intercalated, the Dongyuemiao shale is different due to its abundant shell laminae and interlayers. Due to the lack of studies on shell laminae and interlayers, their influence on oil accumulation is still unclear. This study integrated total organic carbon and X-ray diffraction data, core and thin section observations, field-emission scanning electron microscopy, major and trace element data, and helium porosimetry to investigate the depositional environment and porosity structure of shell interlayers in the shale in the first member of the Dongyuemiao shale (Dong-1 member) and their impact on petroleum accumulation. Results show that Dong-1 member was deposited in a sub-lacustrine fan, and shells and shell fragments were transported by gravity flow. Shells and shell fragments were transported and broken up to under different hydrodynamic conditions, and formed laminae, interlayers, and thick interlayers of shell fragments. In the shell laminae (≤ 1 cm) and thin interlayers (1–10 cm), micro-scale dissolution pores and microfractures formed in the shell clasts can effectively connect the dissolution pores and black shale matrix. The thick shell interlayers (≥ 10 cm) lack porosity networks and prevent petroleum migration. The shell laminae and thin interlayers are the storage space and pathway for petroleum storage and migration, while the thick shell layers are seals that prevent petroleum leakage. This integrated study of a shell-rich shale can provide a reference for petroleum exploration and quantitative evaluation of the resources.

KEYWORDS

shell laminae and interlayer, sedimentary environment, pore structure, petroleum accumulation, Dongyuemiao shale

Introduction

Organic matter-rich shales occur in many lacustrine basins from the Mesozoic and Cenozoic in China, and the resources within those lacustrine basins are one of the sources of unconventional petroleum (Bechtel et al., 2018; Jarvie et al., 2007; Jia et al., 2013; Li et al., 2020). In recent years, exploration wells drilled in the Sichuan Basin, Bohai Bay Basin, Songliao Basin, Ordos Basin, and Junggar Basin have produced commercial oil flows, indicating the high petroleum potential of lacustrine basins (Jia et al., 2012; Li et al., 2015; Liang et al., 2017; Jin et al., 2021; Chen et al., 2023). In lacustrine basins, sediments are more sensitive to tectonic activities, lake-level change, paleoclimate change, and special geological events such as volcano eruption and gravity flow (Bohacs et al., 2000; Chamberlain et al., 2013; Zhang et al., 2017). Many studies have shown that the accumulation of petroleum is co-controlled by lithofacies, pore structure, and occurrence characteristics of shale oil (Chalmers et al., 2012; Xu et al., 2017; Alnahwi et al., 2018). Because lacustrine basins are frequently small in scale and have shallow water depths, lacustrine shales usually form different types of laminae (thickness ≤ 1 cm) and interlayers (thickness > 1 cm). Laminae and interlayers influence petroleum accumulation, but different lacustrine shales show different types of storage space (Milliken, 2003; Wan Hasiyah et al., 2012; Huang et al., 2017; Hua et al., 2020). In addition, lacustrine basins usually receive inputs from multiple sources and experience lateral migration of depocenters so that lacustrine shales can contain multiple types of laminae and interlayers (Desborough, 1978; Doebbert et al., 2010; Liu et al., 2018; Ma et al., 2017).

The Ziliujing Formation in the Sichuan Basin has been reported to have high petroleum potential, and the Dongyuemiao member is one of the two potential targets (the other is the Lianggaoshan member) (Qiu and He, 2021). The Dongyuemiao member can be divided into three members (namely, Dong-1, Dong-2, and Dong-3) (Shu et al., 2021). The black shale in the Dong-1 member is the major petroleum production zone and has good exploration potential in this area, which contain shell interlayers. These freshwater shells were widely distributed across the Paleo-Asian continent (Hu et al., 2021; Shu et al., 2021).

Laminated and interlayered shales have been suggested to be the most favorable lithofacies in petroleum production, for example, the carbonate interlayer in the Eagle Ford shale (Southwestern Texas, United States), laminated carbonate shale in the Shahejie Formation (Bohai bay Basin, China), and laminated felsic shale in the Qingshankou Formation (Songliao Basin, China) (Hua et al., 2022; Shi et al., 2022; Wang et al., 2022). In the Dongyuemiao Formation, abundant shell laminae and interlayers occur throughout the whole section. If it follows the previous petroleum production experience in other laminae and interlayer shale formations, the Dongyuemiao member will be a high-profit target. However, the production behaviors show that the shell laminae and interlayers in the Dong-1 member cannot be simply interpreted to be the “sweet spot” and that petroleum production is still challenging because their influence on the petroleum accumulation, storage, migration, and preservation is still unclear (Zou et al., 2019).

The objective of this study was to investigate the origins and depositional processes of shell layers, the pore characteristics of

different types of shell layers, and their effects on petroleum accumulation in the Dong-1 member. In addition, this study can aid in the location of high-quality Jurassic shale source rocks and accurate evaluation of petroleum resource potential in the Fuxing area.

Geological background

The Sichuan Basin is located on the western margin of the Yangtze plate. It has undergone four stages of tectonic evolution: the Caledonian, Hercynian, Indosinian, and Yanshan-Himalayan. It is bordered by the Micangshan Uplift, Longmenshan fold belt, Dabashan fold belt, Xuefengshan uplift, and Emeishan fold belt (Qiu and He, 2021) (Figure 1A). In the late Triassic, the collision of the Yangtze plate and North China plate transformed the Sichuan Basin from a marine basin to a foreland basin. In the early Jurassic, a set of lacustrine shales (the Dongyuemiao member and the Da'anzhai member of the Ziliujing Formation and the Lianggaoshan Formation) were deposited (Zhang et al., 1996; Meng and Zhang, 1999) (Figure 1B).

The Fuxing area is located in the southern part of the Chuandong high-steep fault-fold belt in the northeast Sichuan Basin. The area is located in a northeast strike syncline region (Bashansi syncline and Liangping syncline), showing two uplifts sandwiched by three sags and a set of preserved Zhendanian–Jurassic rock formations (Figure 1B). The interval of interest is the Dongyuemiao member, which is overlain by the Fuma'anshan member and underlain by the Zhengzhuchong member. The Dongyuemiao member can be subdivided into three members (namely, Dong-1, Dong-2, and Dong-3), of which the black shale in the Dong-1 member is the major petroleum production zone, with an average thickness of 27 m. The Dong-1 member is further divided into four units, which are Unit 1 to Unit 4 from bottom to top (Shu et al., 2021; Peng et al., 2022) (Figure 1C).

Sample and methods

Sample collection and preparation

To study the sedimentary features of organic matter-rich shales and shell layers of the Dong-1 member, a total of 24 samples were collected from the Dong-1 member in the XYA well. This well produced 55.8×10^3 cubic meters of natural gas and 17.6 cubic meters of crude oil per day during production testing. The samples were collected over the depth range of 2,935.6–2,959.5 m with a sampling interval of 0.5–1 m. Twenty-two samples are black shales containing shell laminae and interlayers, whereas XYA 2939.6 and XYA 2942.5 from Unit 3 were collected from thick-layer shell interlayers.

Samples were cut into cubes (1 cm \times 0.8 cm \times 0.5 cm) for field-emission scanning electron microscopy (FE-SEM), and rock fragments from sample cutting were used to make petrographic thin sections. All 24 samples were crushed into 40–60 mesh particles for porosity analyses and into powders for X-ray diffraction (XRD), total organic carbon (TOC), and major and minor element analyses.

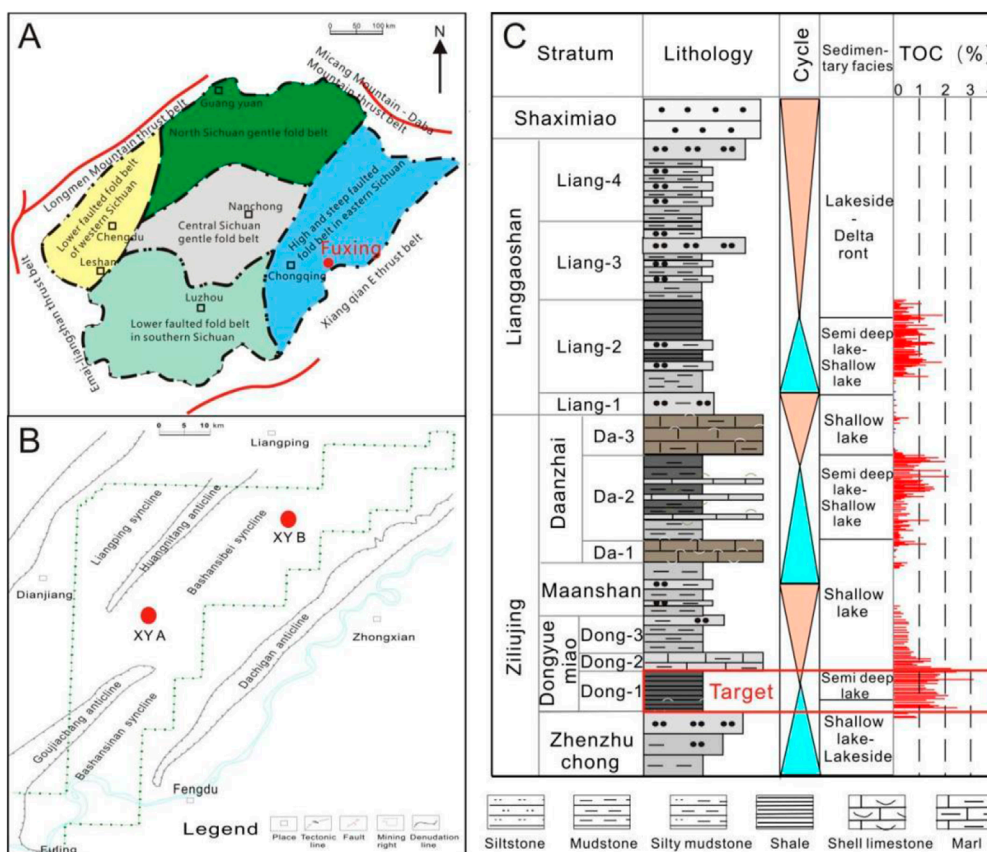


FIGURE 1 Location of the Fuxing area (A), tectonic location map of the Fuxing area (B), and stratigraphic column of Lower Jurassic strata in the Fuxing area (C).

X-ray diffraction

Powder samples were directly analyzed using Bruker D8 Advance to determine bulk mineral compositions. Clay minerals are analyzed separately from bulk mineral, following the procedure of decarbonization, removal of organic matter, ultrasonic shaking, concentration, and XRD scan.

Total organic carbon

Two hundred milligrams of rock powder were first oven dried at 60°C for 12 h and then treated with 10% HCL to remove carbonate minerals at the same temperature. After acid treatment, samples were washed with distilled water to remove residual HCL. Samples were dried again and analyzed using a LECO CS844 Carbon/Sulfur determinator.

Core observation and petrophysical microscopy

Cores samples were observed to roughly determine the lithology and sedimentary features. The thickness and number of shale layers in the Dong-1 member were recorded. Thin sections were made

for a detailed investigation of sedimentary features of shale and shell layers.

Field-emission scanning electron microscopy

Rock samples were cut into pieces measuring 1 cm × 0.8 cm × 0.5 cm and then polished using sandpapers and an argon ion milling machine. Polished surfaces were observed under a Zeiss SUPPA 55 FE-SEM.

Major and trace element analyses

Fifty milligrams of crushed rock particles (75–177 μm) were weighed and placed in a beaker with a few drops of ultrapure water and 2 mL of a mixture of HF and HNO₃ (1:1). The beakers (with sealed tops) were heated for 48 h to evaporate the remaining liquid at 115°C until dry. Then, 2 mL of 2% HNO₃ and 3 mL ultrapure water were added to the beaker; the top was sealed again, and it was heated at 135°C for 5 h. The liquid was transferred to a polyethylene tube and diluted to 100 mL with 2% HNO₃, and then analyzed with inductively coupled plasma mass spectrometry (ICP-MS) to determine the concentrations of major and trace elements.

TABLE 1 TOC and porosity of 24 samples from the XYA well in the Fuxing area.

Sample ID	Unit	Lithofacies	TOC (%)	Porosity (%)	Average of black shales	
					TOC (%)	Porosity (%)
XYA 2935.6	Unit 4	Shell-laminated clay-rich shale	2.6	4.5	2.0	4.1
XYA 2936.6			1.9	4.4		
XYA 2937.5			1.9	4.1		
XYA 2938.7			1.6	3.5		
XYA 2939.6	Unit 3	Shell limestone	0.5	0.9	1.6 (excludes two shell limestones)	4.4 (excludes two shell limestones)
XYA 2940.7		Shell rhythmic clay-rich shale	1.7	4.7		
XYA 2941.5		Silt-shell-laminated clay-rich shale	1.8	4.6		
XYA 2942.5		Shell limestone	0.7	0.9		
XYA 2943.7		Silt-shell-laminated clay-rich shale	1.7	4.2		
XYA 2944.5			1.7	4.5		
XYA 2945.6			1.0	4.2		
XYA 2946.4	Unit 2	Shell rhythmic clay-rich shale	1.1	3.9	1.6	3.7
XYA 2947.7			1.3	4.0		
XYA 2948.7			1.7	2.8		
XYA 2949.7			2.1	3.7		
XYA 2950.7			2.4	4.8		
XYA 2951.7			1.4	4.2		
XYA 2952.7			1.9	4.2		
XYA 2954.6		Shell rhythmic clay-rich shale	1.2	2.1		
XYA 2955.7			1.6	3.7		
XYA 2956.6	Unit 1	Shell rhythmic clay-rich shale	2.1	2.5	1.6	3.1
XYA 2957.5			1.3	3.2		
XYA 2958.4			1.4	2.8		
XYA 2959.5			1.6	4.0		

Helium porosimetry

Samples were analyzed using an Ultrapore-300 helium porosimeter manufactured by Core Laboratories, Wuhan City, Hubei Province, China. The samples were processed into the columns and placed in an oven to be dried at 105°C to remove moisture within the pore spaces. Porosity was analyzed under a helium pressure of 1.387 Mpa (200 psi).

Results

Mineral compositions and organic richness

In the Dong-1 member, the black shales have a TOC of 1.0%–2.6%, with an average of 1.7% (Table 1). In contrast, the two thick shell interlayers exhibit lower TOC values of 0.5% and 0.7%, respectively (Table 1).

TABLE 2 Mineral compositions of 24 samples from the XYA well in the Fuxing area.

Sample ID	Unit	Mineral composition (%)																
		Quartz	Orthoclase	Albite	Calcite	Dolomite	Aragonite	Siderite	Gypsum	Anhydrite	Barite	Hornblende	Pyroxene	Pyrite	Montmorillonite	Illite	Kaolinite	Chlorite
XYA 2935.6	Unit 4	21.1	0.4	2.1	9.1	0.2		0.9	0.1	1.1	0.4	1.0	3.3	1.8	8.4	33.7	6.4	9.9
XYA 2936.6		23.4	0.5	1.9	1.0	0.1		1.2		1.2			3.5	1.9	9.4	37.6	8.5	9.8
XYA 2937.5		23.2	0.5	1.8	14.8	0.7		1.2	0.2	0.7		0.8	2.3	2.8	9.4	28.4	6.6	6.6
XYA 2938.7		24.9	0.3	2.0	2.0	0.2		1.3		1.0	0.7		4.0	1.3	9.2	34.4	8.1	10.6
XYA 2939.6	Unit 3	10.0		0.6	60.4	0.5	4.6	0.3	0.1	0.5	0.5	0.9		2.0	1.9	11.6	2.0	4.1
XYA 2940.7		25.4	0.4	1.9	1.0	0.2		1.6		0.8	0.4	0.6	3.8	1.6	8.7	39.2	7.5	6.9
XYA 2941.5		25.1	0.4	2.0	4.8	0.5		1.1	0.1	0.7		0.8	4.0	1.3	8.3	33.7	7.7	9.5
XYA 2942.5		14.9	0.1	1.0	36.2	7.5		10.1	0.1	0.5		0.6		0.7	2.5	13.4	2.5	9.9
XYA 2943.7	Unit 2	23.1	0.3	1.9	3.3	0.2		1.3	0.2	0.7	0.3		3.0	1.7	9.6	36.4	9.0	9.0
XYA 2944.5		25.1	0.4	2.0	3.6	0.5		0.9		1.2			2.3	1.9	9.1	38.7	8.1	6.2
XYA 2945.6		23.0	0.2	1.4	4.7	0.3		0.7	0.2	0.8	0.4	1.2	2.8	4.8	9.8	36.1	7.1	6.5
XYA 2946.4		19.2	0.4	1.9	19.7	0.7		2.7	0.2	1.1	1.1	1.0	2.5	1.2	6.4	26.4	6.3	9.2
XYA 2947.7	Unit 2	30.1	0.6	2.3	0.4	0.1		1.7	0.2	0.9			4.0	0.4	8.7	33.4	8.3	8.9
XYA 2948.7		27.1	0.5	2.1	0.9	0.1		1.8	0.1	1.4	0.7	0.4	3.8	0.5	9.2	29.6	9.7	12.1
XYA 2949.7		29.7	0.6	2.7	0.3	0.3		1.5		1.5		0.5	4.6	0.2	6.1	30.5	9.3	12.2
XYA 2950.7		26.3	0.5	2.0	0.6	0.3		1.4		1.0		0.9	4.8	1.0	8.4	35.1	8.6	9.2
XYA 2951.7	Unit 2	33.8	0.5	2.2	0.3	0.1		1.2	0.1	0.8	0.5		3.9	0.6	7.6	28.8	10.6	9.0
XYA 2952.7		29.2	0.5	2.1	4.3	0.3		0.9		1.1	0.8		3.9	0.6	7.9	33.2	7.9	7.3
XYA 2954.6		23.9	0.5	2.2	10.3	0.1		1.0	0.1	0.9	0.4		3.4	0.4	5.4	29.3	9.7	12.5

(Continued on the following page)

TABLE 2 (Continued) Mineral compositions of 24 samples from the XYA well in the Fuxing area.

Sample ID	Unit	Mineral composition (%)																
		Quartz	Orthoclase	Albite	Calcite	Dolomite	Aragonite	Siderite	Gypsum	Anhydrite	Barite	Hornblende	Pyroxene	Pyrite	Montmorillonite	Illite	Kaolinite	Chlorite
XYA 2955.7	Unit 1	26.1	0.4	2.0	8.0	0.1		1.2	0.1	1.2		0.8	3.4	0.5	7.1	29.4	10.1	9.6
XYA 2956.6		28.5	0.6	2.2	6.2	0.4		1.4	0.1	1.3	0.3	0.8		1.5	7.9	30.1	9.1	9.6
XYA 2957.5		32.1	0.5	2.2	6.7	0.2		1.3	0.1	1.2			3.4	0.5	9.4	27.4	7.3	7.8
XYA 2958.4		27.0	0.3	2.0	3.0	0.2		1.2		1.2		1.0	4.5	0.3	8.5	30.6	9.5	10.7
XYA 2959.5		27.8	0.7	2.5	5.2			1.4	0.1	1.4			4.5	0.3	5.7	31.3	9.0	10.1

The black shales in the Dong-1 member contain 21.5%–34.8% siliceous minerals, 1.6%–16.7% carbonate minerals, and 48.3%–62.3% clay minerals (Table 2). The two thick shell interlayers are composed of 10.6% and 16.0% siliceous minerals, 65.8% and 53.8% carbonate minerals, and 19.6% and 28.3% clay minerals, respectively (Table 2).

Lithofacies and sedimentary features

Four lithofacies can be distinguished in the Dong-1 member based on the sedimentary texture and mineral compositions. These are shown in Figure 2: (1) shell-laminated clay-rich shale, (2) silt-shell-laminated clay-rich shale, (3) shell rhythmic clay-rich shale, and (4) shell limestone. The shell-laminated clay-rich shale contains mm-thick shell laminations, with an average layer frequency of 65 shell laminations/m. This lithofacies has a clay mineral content >50% and mainly occurs in Unit 4. The silt-shell laminated clay-rich shale also has a clay content >50% and contains interbedded siliceous laminae and shell laminae, with an average frequency of 110 laminations/m and 53 laminations/m, respectively. This face occurs mainly in Unit 3 and the upper-middle part of Unit 2. The shell rhythmic clay-rich shale occurs in Unit 1 and the lower part of Unit 2. The frequency of the shell interlayer is variable through the section, with an average layer density of 70 laminations/m. The shell limestone appears from Unit 1 to Unit 3, and the shell interlayer accounts for more than 90% of the shell limestone. It is worthwhile noting that in Unit 3, two shell limestone layers whose thicknesses are 80 cm and 25 cm are used as marker layers because of their greater thickness.

A large number of shell layers (laminae and interlayers), with thickness ranges from 1 mm to 50 cm, occur in the Dong-1 member. The shell layers in Unit 1 show normal and reverse rhythms. The normal rhythm shows the thicknesses of the shell layers, and the areal ratios of shell layers/black shell matrix increase from bottom to top, and the spacing between two shell layers decreases (Figure 3). In the reverse rhythm, the thicknesses of the shell layers and the areal ratios of shell layers/black shell matrix decrease from bottom to top, and the spacing between two shell interlayers increases (Figure 3). In Unit 2, shell layers of 1–10 cm that show sharp boundaries with the black shale matrix were deposited. Thin-section observations show that the voids between shell clasts are filled with the black shale matrix (Figure 3). However, in the upper part of Unit 2, two thick layers of shell interlayers, whose thicknesses are 80 cm and 25 cm, respectively, were deposited. In these two thick shell interlayers, the black shale matrix does not in-fill the voids between shell clasts (Figure 3). In Unit 4, shell laminae were mainly deposited (Figure 3).

Classification of calcite types in shell clasts

Thin-section observations identified six types of calcite: (1) C1: shell without diagenesis, (2) C2: shell with diagenesis, (3) C3: sparry calcite growths along the edge of shell clasts, (4) C4: fibrous calcite growths along the edge shell clasts, (5) C5: micrite, and (6) C6: sparry calcite in-filling the pores and fractures within the shell-rich carbonate rock (Figure 3).

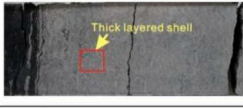
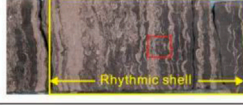
Member	Lithofacies	Unit	Core photograph	Thin section
Dong-1 Member	Shell laminated clay-rich shale	Unit4		
	Slit-shell laminated clay-rich shale	Unit2		
	Shell limestone	Units 1-3		
	Shell rhythmic clay-rich shale	Units 1-4		

FIGURE 2
Characteristics of shell interlayers in shale of different units in the well XYA.

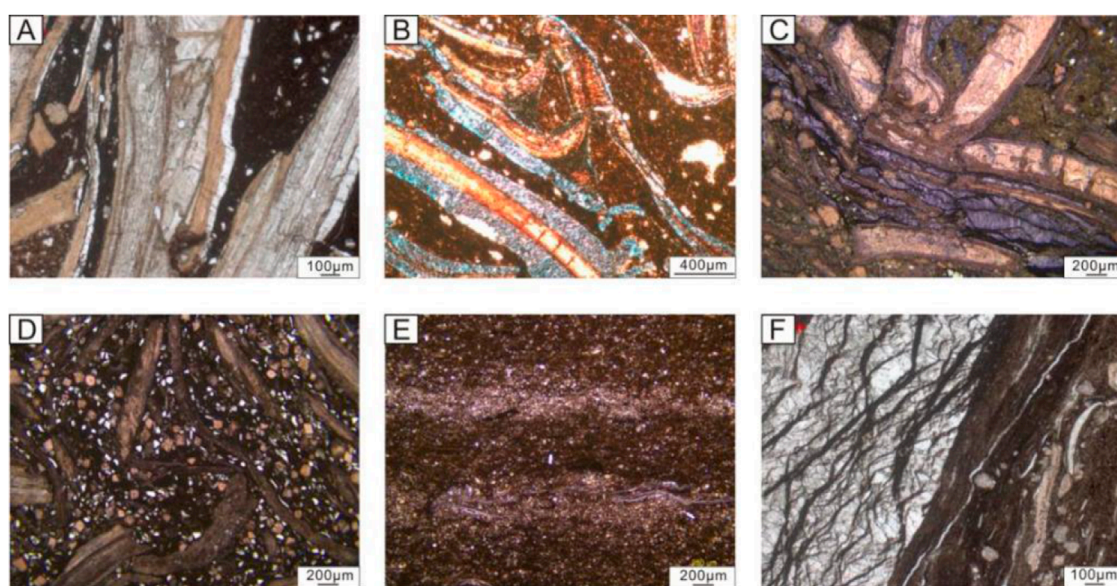


FIGURE 3
Thin section photos of six calcite types in the shell interlayer of the Dong-1 member in well XYA: (A) fine to medium calcite, (B) the micro-sparry calcite distributed along the edge of the scale limestone, (C) fibrous calcite with a vein–lens distribution along the margin of the shell interlayer, (D) clastic particles of the shell, (E) micritic calcite, and (F) sparry calcite with late filling of pores/fractures in the shell interlayer and filling of pores/fractures in shell limestone along the margin of shell limestone vein–lens distribution along the margin of shell limestone.

C1 is the body of the shell that has not experienced diagenesis. However, shells are prone to break under compression. C2 is a subangular rhomboid to irregular polygon in shape, exhibits slight dolomitization, and appears to have been affected by the crushing process of storms. C3 shows sharp contact surfaces with shells and does not contain obvious dissolution pores. C4 shows dark-colored axes in the middle of crystals, which are identified as oil by showing blue to blue-purple color after staining. C5 is mainly microcrystalline calcite in carbonate-rich shales. C6 is light-colored

in-fill of fractures and pores, and can be seen in the cores. The dark-colored axis can be seen in the minerals by the naked eye.

Major and trace elements

In the black shales, the most abundant major elements are Al_2O_3 , Fe_2O_3 , and K_2O , with average concentrations of 19.82%, 6.98%, and 3.57%, respectively. The concentrations of CaO and MgO

TABLE 3 Major element contents of 24 samples from the XYA well in the Fuxing area.

Sample ID	Unit	Major element (%)							
		Al ₂ O ₃	CaO	Fe ₂ O ₃	K ₂ O	MgO	MnO	Na ₂ O	TiO ₂
XYA 2935.6	Unit 4	19.42	5.14	7.53	3.65	2.11	0.04	0.55	0.75
XYA 2936.6		20.17	1.18	6.52	3.91	1.93	0.03	0.65	0.74
XYA 2937.5		19.19	6.98	6.30	3.25	1.72	0.04	0.59	0.73
XYA 2938.7		21.16	2.44	7.13	3.82	2.10	0.04	0.63	0.71
XYA 2939.6	Unit 3	6.98	37.74	3.03	1.17	0.89	0.04	0.20	0.22
XYA 2940.7		20.00	1.34	6.23	3.69	1.90	0.03	0.59	0.81
XYA 2941.5		19.60	3.32	6.71	3.57	2.08	0.04	0.56	0.79
XYA 2942.5		7.42	25.03	12.78	1.21	2.80	0.22	0.18	0.26
XYA 2943.7		20.74	1.91	7.42	3.54	2.09	0.04	0.60	0.77
XYA 2944.5		20.64	2.57	6.50	3.54	1.94	0.04	0.58	0.72
XYA 2945.6		20.49	3.92	7.31	3.50	1.78	0.04	0.57	0.71
XYA 2946.4		16.78	13.41	6.62	3.05	1.91	0.05	0.48	0.61
XYA 2947.7		19.76	0.45	6.41	3.57	1.98	0.03	0.64	0.92
XYA 2948.7		20.13	2.28	7.13	3.67	2.05	0.04	0.55	0.86
XYA 2949.7	Unit 2	19.71	0.42	7.52	3.79	2.14	0.04	0.60	0.89
XYA 2950.7		20.45	0.81	7.13	3.82	2.07	0.04	0.54	0.91
XYA 2951.7		18.98	0.38	6.45	3.28	1.90	0.03	0.60	1.02
XYA 2952.7		19.69	1.73	6.54	3.57	1.92	0.04	0.57	0.94
XYA 2954.6		19.32	4.58	8.10	3.58	2.04	0.06	0.52	0.80
XYA 2955.7		20.37	1.49	7.31	3.58	2.01	0.06	0.60	0.87
XYA 2956.6		20.60	1.77	7.19	3.71	2.02	0.04	0.57	0.90
XYA 2957.5	Unit 1	18.30	4.75	6.71	3.09	1.83	0.05	0.63	0.88
XYA 2958.4		19.97	1.22	7.62	3.63	1.97	0.04	0.50	0.89
XYA 2959.5		20.63	1.55	7.20	3.76	2.06	0.05	0.58	0.94

average 2.89% and 1.98%, respectively, whereas the concentrations of MnO, Na₂O, and TiO₂ are less than 1%. In contrast, the two thick shell interlayers have higher average CaO and Fe₂O₃ concentrations than the black shales (31.39% and 7.90%, respectively), but lower concentrations of other major elements (Table 3).

The analytical data show that there are significant differences in the concentrations of trace elements between black shales and the two thick shell interlayers. The black shales have 1.45–3.44-times higher average concentrations of all trace elements, except Sr, than the two thick shell interlayers. The two thick shell

interlayers have 5.17-times higher average Sr concentration than the black shales (Table 4).

Porosity and pore types

The porosity of the black shale ranges from 2.1% to 4.8%, and the porosity of two thick shale interlayers is 0.9% (Table 1). Shales in Unit 3 have the highest average porosity of 4.4%, whereas the shales in Unit 4 and Unit 2 have average porosities of 4.1% and

TABLE 4 Trace element contents of 24 samples from the XYA well in the Fuxing area.

Sample ID	Unit	Trace element (µg/g)												
		Ba	Co	Cr	Cu	Li	Ni	Sr	V	Zn	Zr	La	Th	U
XYA 2935.6	Unit 4	689.03	17.71	110.86	56.83	66.53	51.20	192.33	157.28	175.35	137.82	30.75	14.54	2.74
XYA 2936.6		764.27	14.96	122.33	55.35	72.78	50.01	158.76	193.81	166.11	132.52	25.04	11.44	2.35
XYA 2937.5		671.28	14.91	105.42	53.88	68.82	39.95	277.90	163.82	156.35	130.03	27.64	13.57	2.66
XYA 2938.7		878.42	14.89	116.22	58.76	66.41	47.85	176.36	162.59	192.82	134.91	31.37	14.81	2.58
XYA 2939.6	Unit 3	686.63	7.59	43.95	16.84	22.19	20.64	1,114.94	55.69	61.99	44.95	11.39	4.61	1.06
XYA 2940.7		782.15	16.85	119.09	63.14	78.63	53.38	177.05	169.25	139.96	147.19	31.48	14.69	2.71
XYA 2941.5		774.08	15.51	116.55	57.10	73.48	47.04	181.80	163.08	135.47	158.34	33.35	15.34	3.07
XYA 2942.5		383.00	6.62	43.43	21.85	32.26	22.87	658.92	78.56	62.19	48.70	13.29	4.83	1.73
XYA 2943.7		788.97	18.02	116.15	50.04	78.46	50.28	170.72	181.48	184.86	133.40	27.50	12.57	2.59
XYA 2944.5		816.73	16.61	119.41	53.77	68.13	44.47	169.28	173.58	129.72	130.98	27.68	12.73	2.49
XYA 2945.6		792.67	20.05	113.67	54.82	64.97	47.66	184.01	182.95	158.82	135.27	29.42	15.15	2.91
XYA 2946.4		697.09	19.03	95.31	52.79	67.86	43.94	308.84	134.18	109.27	118.36	30.96	15.12	2.46
XYA 2947.7	Unit 2	757.92	17.69	122.38	59.42	85.16	51.19	127.93	166.59	164.41	181.54	37.58	19.65	3.43
XYA 2948.7		828.36	21.41	116.98	66.93	88.80	53.04	166.17	166.00	222.91	170.09	48.95	22.89	3.91
XYA 2949.7		808.72	18.76	118.63	64.63	97.95	57.02	127.30	173.67	153.57	170.24	34.87	19.84	3.38
XYA 2950.7		835.56	18.45	123.42	61.40	94.12	55.03	125.48	169.82	154.68	177.48	36.06	17.42	3.40
XYA 2951.7		724.31	16.66	117.21	75.31	88.37	56.11	121.10	156.42	159.37	200.36	41.08	23.69	3.77
XYA 2952.7		803.93	19.56	123.37	84.45	87.86	57.25	163.92	168.66	208.62	187.59	51.67	28.52	4.88
XYA 2954.6		771.29	15.69	112.93	53.29	83.35	45.60	197.02	157.66	134.25	159.27	36.76	19.50	3.33
XYA 2955.7		Unit 1	803.92	21.55	125.45	56.88	98.11	58.54	148.92	175.51	163.95	184.23	38.43	18.01
XYA 2956.6	863.76		19.91	122.99	69.73	85.32	56.52	138.78	178.89	142.55	180.96	37.09	20.24	3.94
XYA 2957.5	694.23		19.82	113.66	68.85	83.22	55.80	196.24	158.72	153.93	201.06	42.61	21.24	4.20
XYA 2958.4	787.94		19.00	123.10	78.69	106.15	59.60	130.13	187.05	160.24	184.52	38.70	18.98	4.02
XYA 2959.5	817.20		19.97	123.74	70.98	86.64	60.11	132.05	175.39	164.40	191.83	37.51	18.00	3.46

3.7%, respectively. The shales in Unit 1 have the lowest average porosity of 3.1% (Figure 2).

The FE-SEM data show that the porosity of the shales is mainly composed of clay mineral intergranular pores, with a small number of organic matter pores and microfractures (Figure 4). However, in the shell layers, the intergranular pores dominate the porosity. Some intergranular corrosion pores are filled with organic matter, along with the microfractures that connect the intergranular corrosion pores (Figure 4).

Discussion

Sedimentary environment of the Dong-1 member

Paleo-redox and paleo-salinity conditions

The paleo-redox condition has been proven to be one of the important parameters for evaluating organic matter accumulation (Calvert and Pedersen, 1993; Dean et al., 1997; Tribouillard et al.,

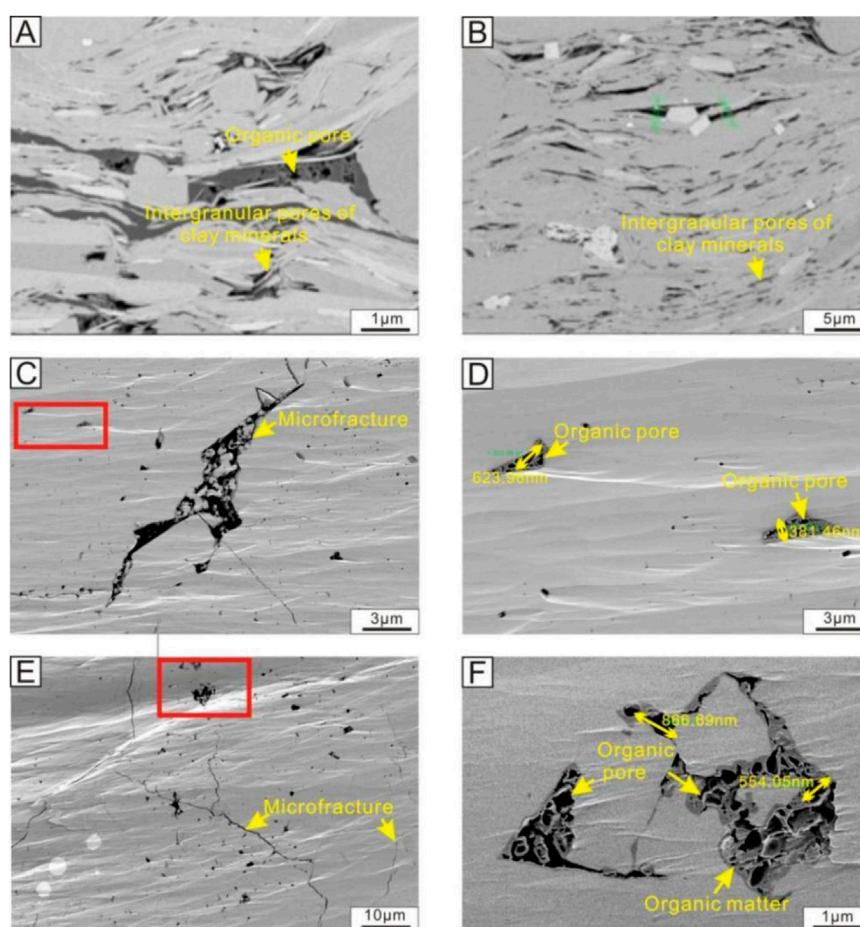


FIGURE 4
SEM images of pores and organic matter in lacustrine shales and shell interlayers. (A) Organic pore and intergranular pores of clay minerals, (B) intergranular pores of clay minerals, (C) microfracture, (D) organic pores, (E) microfractures, (F) organic pores.

2006). Preservation of organic matter is favored in aerobic environments compared to oxidation environments. Previous research has demonstrated that the elements V and Ni are more likely to accumulate in shales deposited in a reducing environment (Feng et al., 2011; Chen et al., 2016). In a highly reducing environment, V has a higher enrichment factor coefficient than Ni, whereas V and Ni show similar enrichment factor coefficients in an oxidizing environment. The stronger the reducing conditions, the higher will be the value of $w_{(V)}/w_{(V+Ni)}$, where W is the weight percentage. Consequently, the value is used to indicate an anaerobic environment (>0.84), an anoxic environment (0.6–0.84), and an aerobic environment (<0.6). (He et al., 2022a). Results show that the $w_{(V)}/w_{(V+Ni)}$ value of the Dong-1 member ranges from 0.73 to 0.8 (Figure 5), indicating an anoxic environment during deposition (Lin et al., 2008). Generally, it shows no obvious value changes among the shales in Units 1–4, and only the two thick shell interlayers in Unit 3 have lower values. Three types of lithofacies, namely, shell-laminated clay-rich shale, silt-shell-laminated clay-rich shale, and shell rhythmic clay-rich shale, are mainly deposited in deepwater areas, whereas the lithofacies of shell limestone is deposited in shallow-water areas.

Lake paleo-salinity strongly influences the biochemical processes in the water body and is an important parameter controlling the accumulation of organic matter in shale (Wei et al., 2018; Wei and Algeo, 2019). Usually, high-salinity lake water is related to high productivity, and moderate salinity is beneficial for the preservation of organic matter (Schenau et al., 2001; Tribouvillard et al., 2006; Wu et al., 2019). The Sr/Ba ratio is a key factor in estimating the paleo-salinity of lacustrine sediments. When the salinity increases, Ba precipitates as $BaSO_4$. As evaporation proceeds and water concentration increases, Sr precipitates as $SrSO_4$. According to the Sr/Ba ratio, water salinity can be classified to be fresh water (<0.5), brackish water (0.5–1), and saline water (>1) (He et al., 2022b; Wei and Algeo, 2019). Results show that the Sr/Ba ratio during black shale deposition ranges from 0.15 to 0.44 (Figure 4). The two thick shell interlayers in Unit 3 exhibit a much higher ratio of 1.6 and 1.7, indicating that they were deposited in an evaporative saline water environment. After removing the two thick shell interlayer outliers, there is no significant difference in paleo-salinity among different lithofacies, and the average ratio is 0.21, indicating that the lake contained fresh water during deposition. This is consistent with the paleo-redox index (Table 4).

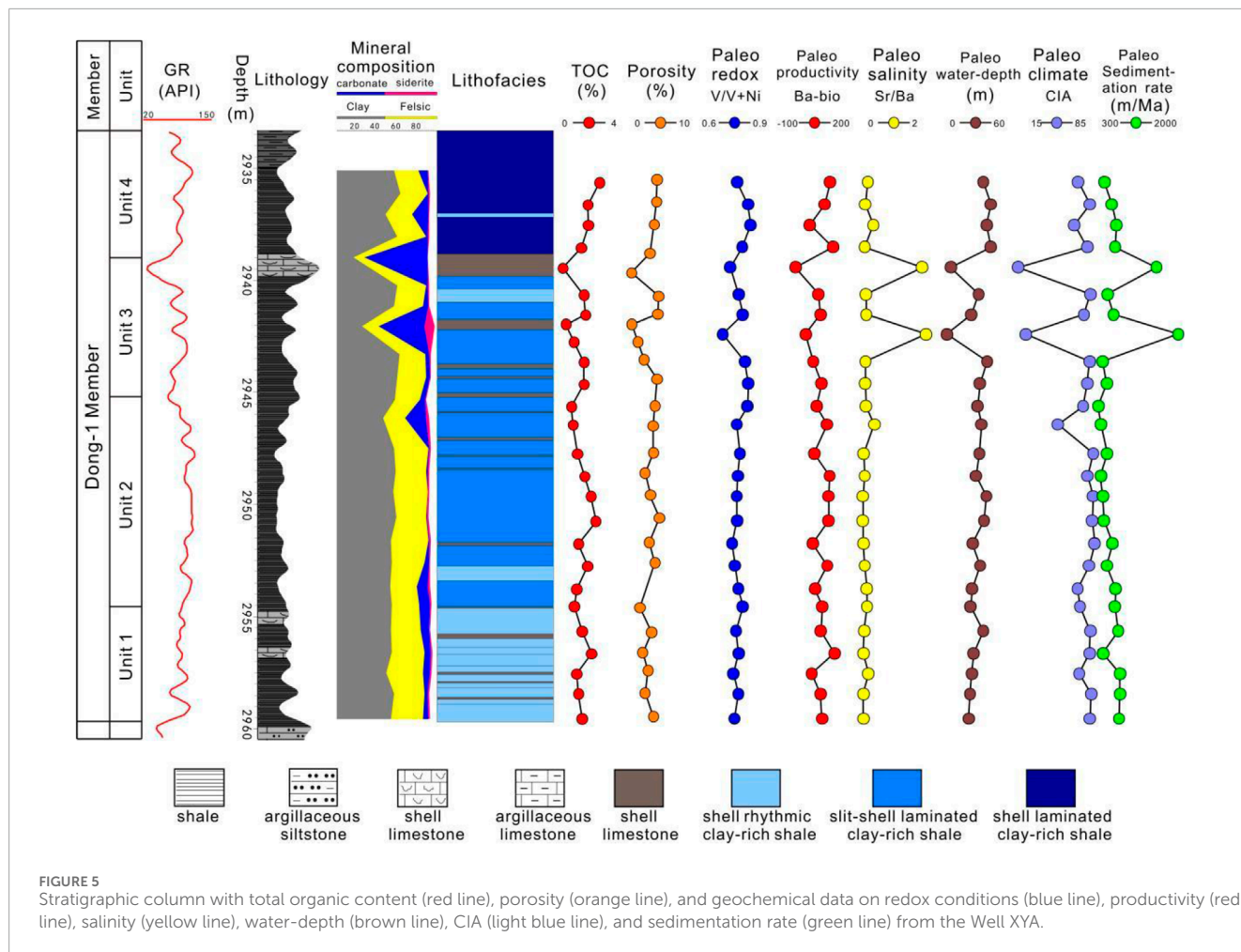


FIGURE 5 Stratigraphic column with total organic content (red line), porosity (orange line), and geochemical data on redox conditions (blue line), productivity (red line), salinity (yellow line), water-depth (brown line), CIA (light blue line), and sedimentation rate (green line) from the Well XYA.

Paleoclimate and paleo-productivity conditions

Changes in paleoclimate influence parent rock weathering, sediment transport, and preservation conditions of organic matter. A warm and humid climate accelerates the circulation of atmospheric water, enhances primary productivity, and favors the burial of organic matter. The major and trace element concentrations can indicate the intensity of parent rock weathering in its provenance and the changes in Paleoclimate during deposition (Nesbitt et al., 1996; Zhang et al., 2005; Chen et al., 2011). The chemical index of alteration (CIA) has been used to reconstruct the paleoclimate, as shown in Equation 1 (He et al., 2022a):

$$CIA = Al_2O_3 / (Al_2O_3 + CaO^* + Na_2O + K_2O) \times 100, \quad (1)$$

where CaO^* is calculated using McLennan's method (McLennan, 1993; Bai et al., 2015).

A CIA larger than 85 indicates that the paleoclimate was tropical and humid and the intensity of parent rock weathering. A CIA between 65 and 85 indicates a warm and humid climate and that the intensity of parent rock weathering was moderate. CIA values less than 65 indicate a cold, arid climate and that the intensity of parent rock weathering is low (Nesbitt and Young, 1989; Nesbitt et al., 1996). The CIA values of the two thick shell interlayers in Unit 3 are very low (15.1 and 21.9), indicating a cold and arid climate (Figure 5; Table 4). In contrast, the CIA values of remainder of the

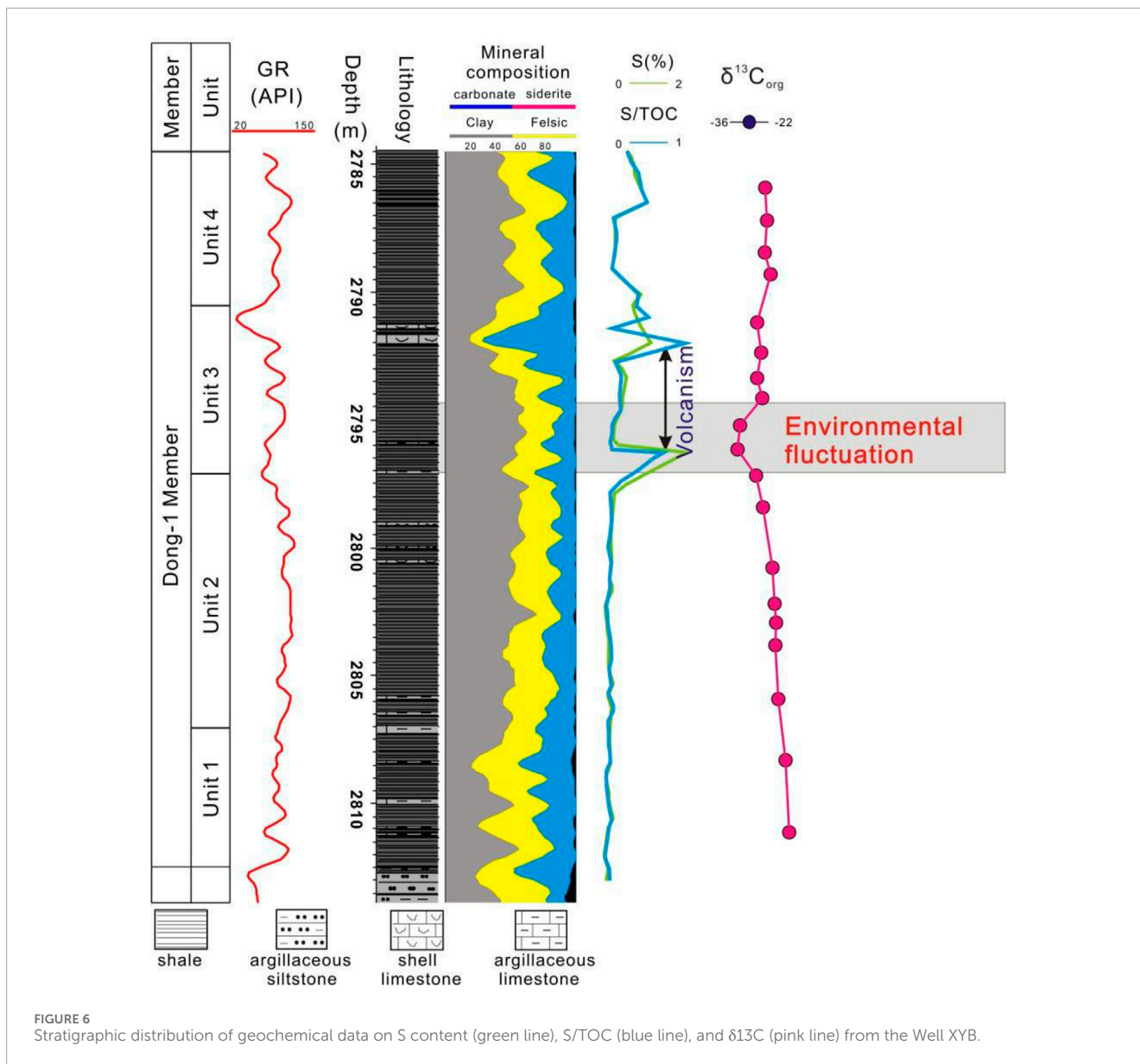
Dong-1 member range from 64.0 to 81.6, indicating a warm and humid climate with moderate rock weathering. This paleoclimate is favorable for primary productivity and organic matter preservation.

Paleo-productivity is an important factor in controlling the organic matter content and petroleum generation potential of sediments. High intensity of photosynthesis increases bioactivity and accelerates the carbon cycle, resulting in high paleo-productivity (Liu et al., 2016; Lu et al., 2019; Wang et al., 2019). This study used the Ba-bio index to evaluate the paleo-productivity (Lu et al., 2019). The Ba element in shale usually originates from two potential sources: (1) biogenetic Ba comes from organic matter of plankton and barite ($BaSO_4$) from bioclasts and (2) extrinsic Ba charge from terrestrial sources (Katz, 1995; Ding et al., 2016). The Ba-bio index can be calculated using Equation 2:

$$Ba_{bio} = Ba_{sample} - Al_{sample} \times (Ba/Al)_{PAAS} \quad (2)$$

where Ba_{sample} and Al_{sample} are the weight percentages in rock samples, PAAS is post-Archean Australian shale, and $(Ba/Al)_{PAAS}$ is a constant of 0.0068 (Thomson et al., 1998; Tribouillard et al., 2006).

The result of the Ba-bio calculation shows that the paleo-productivity of the shell-laminated clay-rich shale is 97.4 ppm, which is the highest in Unit 4 among the four lithofacies. The silt-shell laminated clay-rich shale and the shell rhythmic clay-rich shale have lower paleo-productivities (76.6 and 50.4 ppm,



respectively), whereas the shell limestone has the lowest paleo-productivity (29.0 ppm) (Figure 5; Table 4).

Sedimentation rate and paleo-water depth

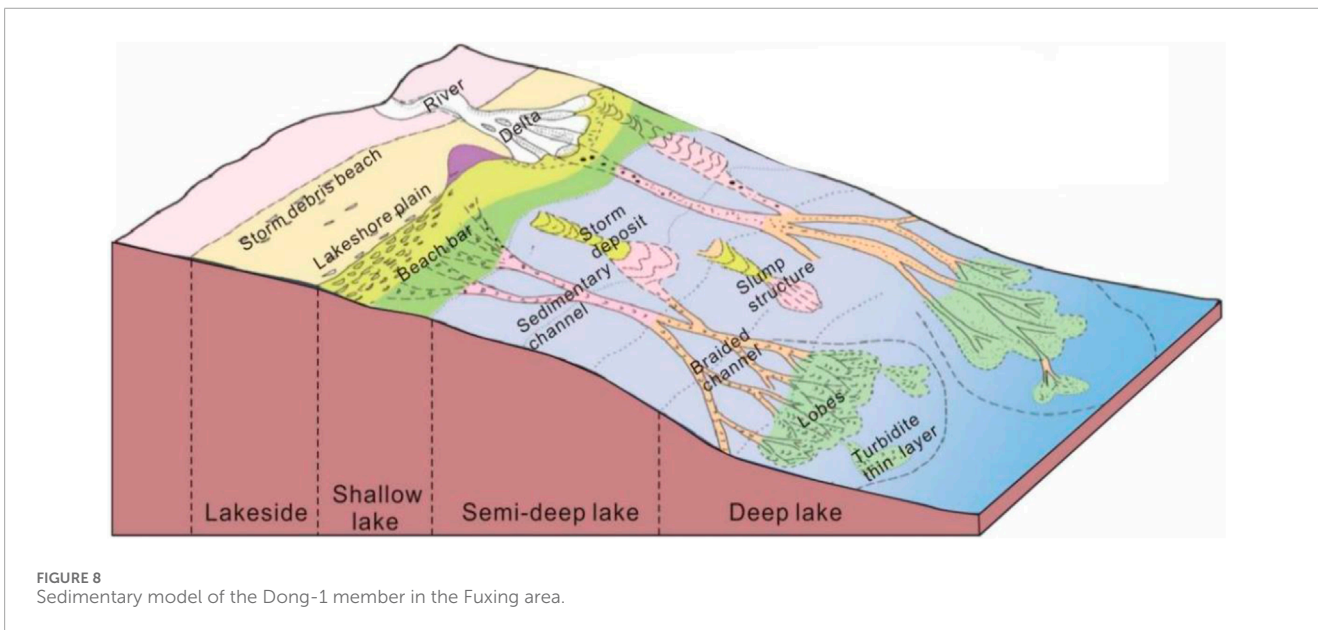
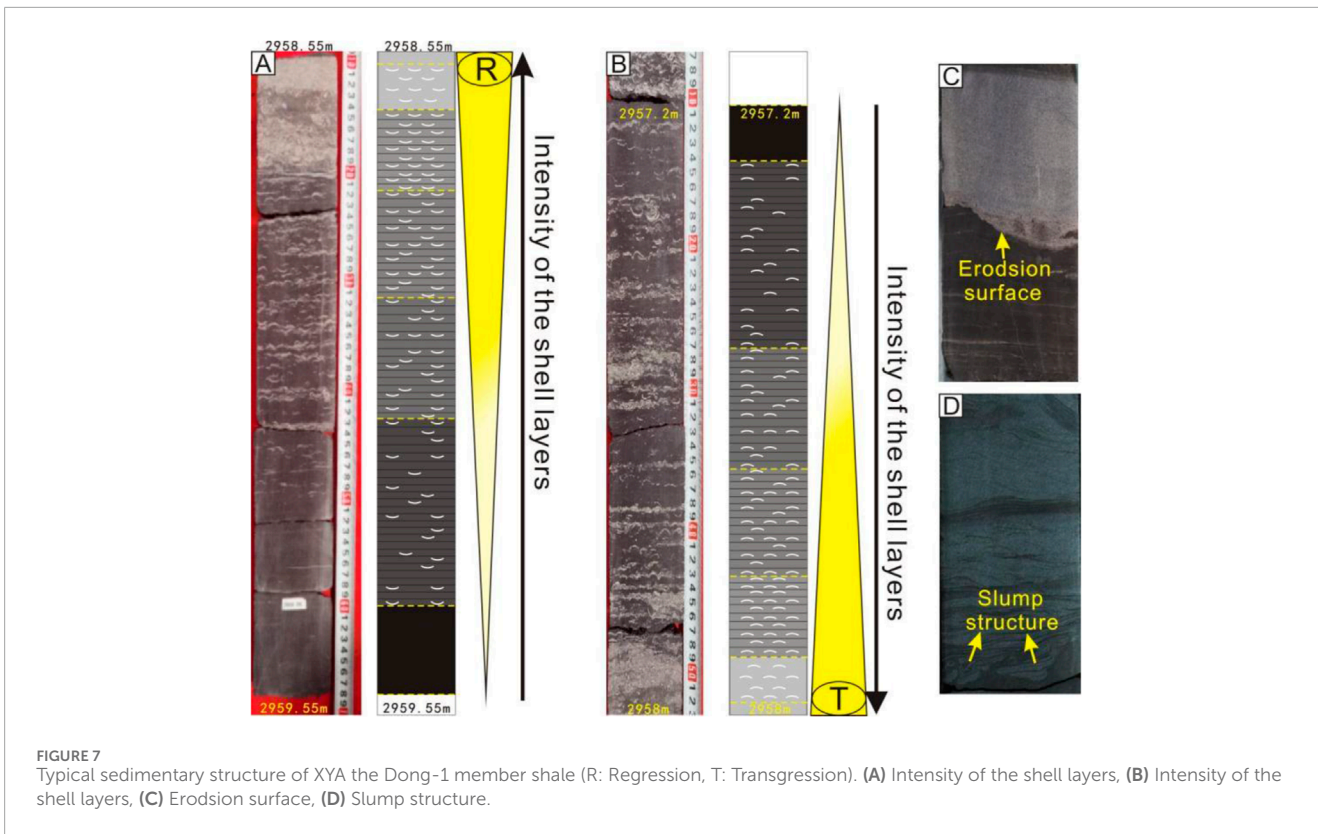
In this study, we reconstructed paleo-water-depth changes during deposition processes by analyzing cobalt (Co) and rare elements in sediments using the method proposed by Zhou et al. (1995). The sedimentation rate was calculated with Co, and the paleo-water depth was calculated with La and Co, using Equations 3 and 4:

$$V_s = V_0 \times \frac{N_{Co}}{(S_{Co} - t \times T_{Co})}, \tag{3}$$

$$H = 3.05 \times \frac{105}{(V_s^{3/2})}, \tag{4}$$

where V_s is the sedimentation rate during rock deposition, V_0 is the sedimentation rate of lake sediments (usually 150–300 m/Ma; this study uses 300 m/Ma), N_{Co} is the Co concentration of lake sediments, S_{Co} is the Co concentration in rock samples, t represents the influence of terrigenous Co on the sample [ratio of La in rock: La (38.9×10^{-6}) in charged sediments], T_{Co} is a constant (4.68×10^{-6}), which represents the concentration of charged sediments, and H is the deepest water depth of the lacustrine basin.

As shown in Figure 5, the sedimentation rate and paleo-water depth show a similar trend. The shell-laminated clay-rich shale was deposited in the deepest water depth (average paleo-water depth: 38.1 m; average sedimentation rate: 490 m/Ma). The silt-shell-laminated clay-rich shale and the shell rhythmic clay-rich shale were deposited in a shallower water depth (average paleo-water depth: 30.4 and 29.1 m; average sedimentation rate: 450 and 566 m/Ma, respectively). The shell mudstone was deposited in the



average paleo-water depth of 25.9 m, and the average sedimentation rate is 588 m/Ma. The shell limestone was deposited in the shallowest paleo-water depth of 23.9 m, with an average sedimentation rate of 637 m/Ma. The two shell limestones were deposited in the paleo-water depth of 10.1 and 7.3 m, with average sedimentation rates of 964 and 1,194 m/Ma. The results of paleo-water depth and the sedimentation rate are well matched with paleo-redox conditions, paleo-salinity, paleo-productivity, and the paleoclimate. There is a

significantly higher degree of variability in every parameter of Shell-1 and Shell-2 in Unit 3 than that of other intervals. This variability suggests that the depositional environment changed abruptly, either due to special geological events (such as volcano eruptions or gravity flow) or a rapid decrease in lake levels. The Shell-1 and Shell-2 intervals deposited in shallow water were exposed to the oxidizing environment, and the paleo-productivity was low, resulting in a low amount of organic matter accumulation.

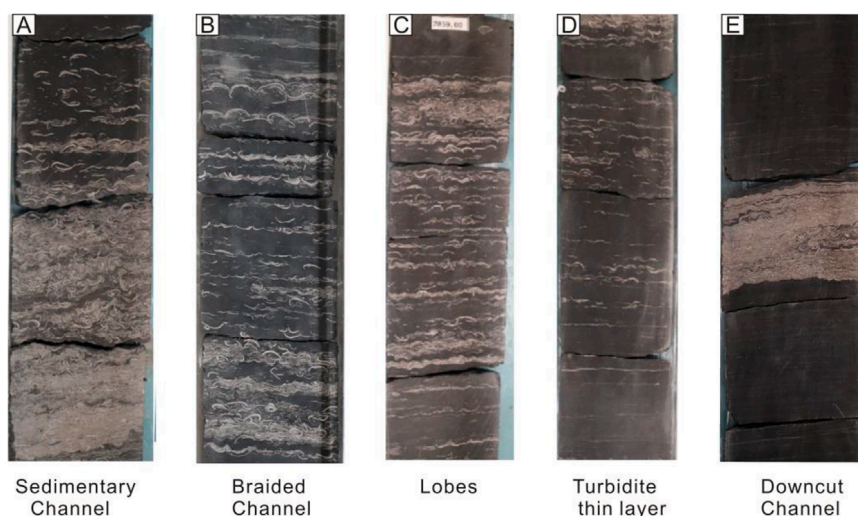


FIGURE 9 Core pictures of five sedimentary microfacies of XYA Dong-1 member (T: Transgression, R: Regression). (A) Sedimentary channel, (B) braided channel, (C) lobes, (D) turbidite thin layer, (E) downcut channel.

Sedimentary history of the Dong-1 member

The previous sedimentary environment analyses indicate that the Dong-1 member was deposited under a warm and humid climate with moderate weathering, and the lake level was getting deeper, forming an overall deepwater anoxic environment, as indicated by the value of $wt.V/wt.V+Ni$ and paleo-water depth. However, the deposition period of two thick shell interlayers in Unit 3 show different properties, indicating that the sedimentary environment has changed.

Special geological events such as glacial period, volcanic eruptions, and tectonic activities make the sedimentary environment change abruptly (Algeo et al., 2016; Langmann et al., 2010; Lu et al., 2019). Previous research indicates that during the early Jurassic (201–174 Ma), the violent emplacement and eruption of Central Atlantic magmatic province (CAMP) abruptly changed the climate and sedimentary environment. The release of volcanic greenhouse gases from CAMP turned the water to be anoxic (Lamotte et al., 2015; Zhang et al., 2022a; Zhang et al., 2022b). Marisa et al. (2020) and Marco et al. (2022) investigated the continuous $\delta^{13}C_{org}$ and pollen records of early Jurassic, indicating that carbon isotope excursions toward lower values in whole-rock carbonates dated from the Sinemurian/Pliensbachian boundary; Davoei, Margaritatus, and Spinatum zones; and possibly from the Pliensbachian–Toarcian boundary (Marisa et al., 2020; Marco et al., 2022). Schöllhorn et al. (2020), Lindström et al. (2019), and Lindström et al. (2021) found that the volcanic eruption caused the carbon isotope negative offset, which is related to the concentration of Hg (Schöllhorn et al., 2020; Lindström et al., 2019; Lindström et al., 2021). Moreover, analysis of the Dong-1 member of the XYB well (10 km away from XYA) reveals that the changes in S/TOC and $\delta^{13}C_{org}$ vs depth indicate a negative offset in $\delta^{13}C_{org}$ and abnormally high S/TOC values immediately before the thicker shell interlayer deposition. As important information retained in sedimentary records, the composition and distribution of carbon isotopes can well reflect

the paleo-climate, paleo-productivity, and burial rate of organic matter (Hatch et al., 1987; Liu et al., 2021; He et al., 2021). The carbonate isotope of kerogen $\delta^{13}C_{org}$ in Unit 3 shows a short negative offset ($>3\text{‰}$), which was thought to be influenced by a volcanic eruption (Figure 6). However, there is no evidence of volcanic eruption during the deposition of the Dong-1 member. Therefore, a possible explanation for this abrupt environmental change is the deposition of the thick shell interlayer under the influence of the middle and remote volcanic activities; the greenhouse gas covered a large area, the oxygen concentration decreased, and the shell organisms massively died and were transported to the deposition area.

Overall, during the deposition of the Dong-1 member, climate changes and geological events resulted in significant variations in the depositional environments of the lacustrine basin in the Fuxing area. From Unit 1 to the middle of Unit 3, the basin deepened slowly and formed the lithofacies of shell-laminated clay-rich shale and silt-shell-laminated clay-rich shale. During the deposition of the middle section of Unit 3, this area was influenced by volcanic activities, and the climate changed from warm and humid to dry and cold conditions. The lake shrank rapidly, the lake level decreased, and the water body became shallower. These events corresponded to the first thick shell interlayer of 25 cm and thus formed the lithofacies of the shell limestone. Subsequently, the climate returned to warm and humid conditions, the lake expanded and deepened, and the lithofacies reverted to shale and shell rhythmic interlayer for a short duration, forming the lithofacies of the shell rhythmic clay-rich shale. However, volcanic events that occurred at the top of Unit 3 led to another round of rapid lake shrinkage. The climate conditions suddenly changed from a warm and humid climate to a dry and cold climate, with a lack of oxygen that cannot meet the conditions for the survival of the shell, resulting in a large number of shell deaths and sedimentation in water bodies. The extreme climate conditions led to a significant die-off of the bivalves, and a large amount of shell was deposited as the second thick interlayer (80 cm). At the

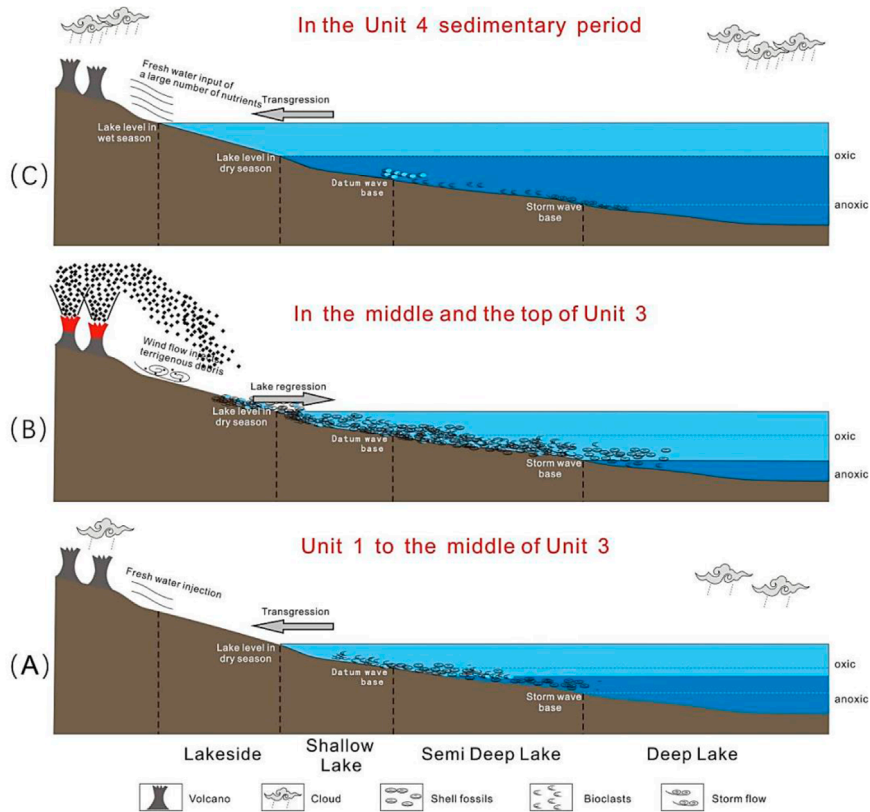


FIGURE 10 Model of sedimentary environment evolution during the Dong-1 member period in the Fuxing area. **(A)** Depositional scheme of the Unit 1 to the middle of the Unit 3, **(B)** depositional scheme of the the middle and the top of the Unit 3, **(C)** depositional scheme of the the Unit 4.

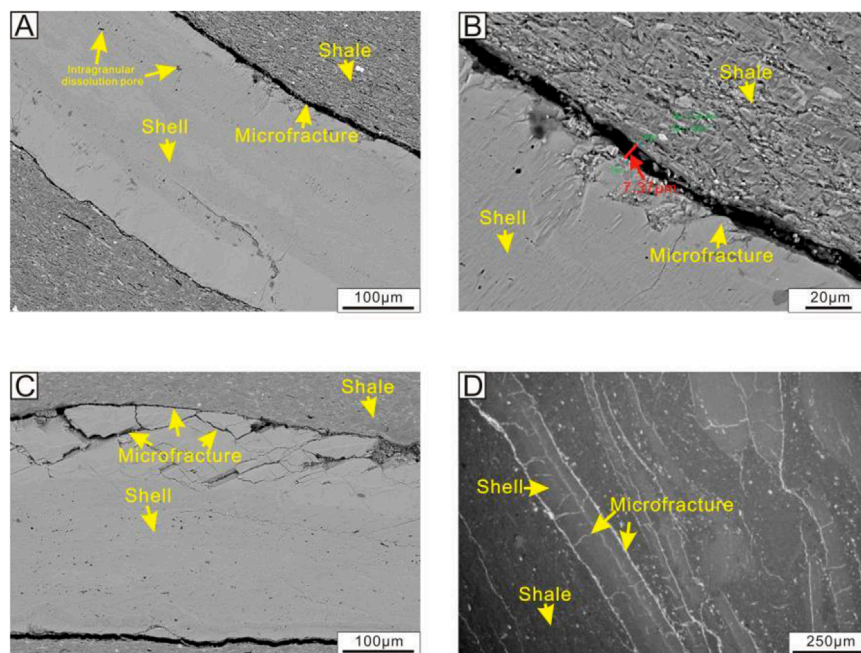


FIGURE 11 SEM images of microfRACTURES between the shell and mudstone in the lacustrine shale and of microfRACTURES formed inside the shell: **(A)** microfRACTURES between the shell laminae and shale, **(B)** enlarged image: microfRACTURES exist between the shell lamella and shale, **(C)** edge of the shell recrystallized to form microfRACTURES, and **(D)** microfRACTURES form inside the shell.

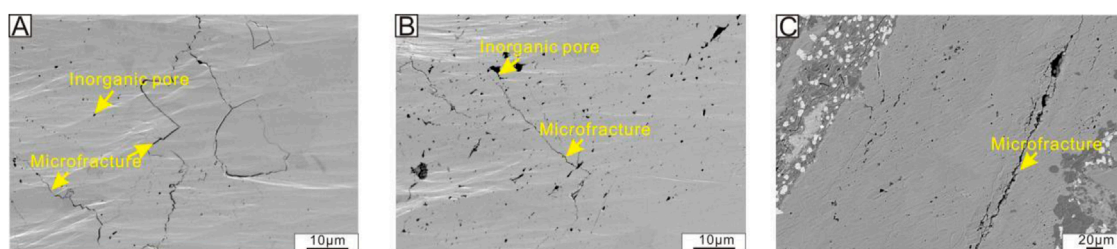


FIGURE 12
SEM images of the microfractures in the shell layer connect dissolution pores. (A) Microfractures and pores connected to them, (B) pores connected to the microfracture and isolated pores, (C) microfracture.

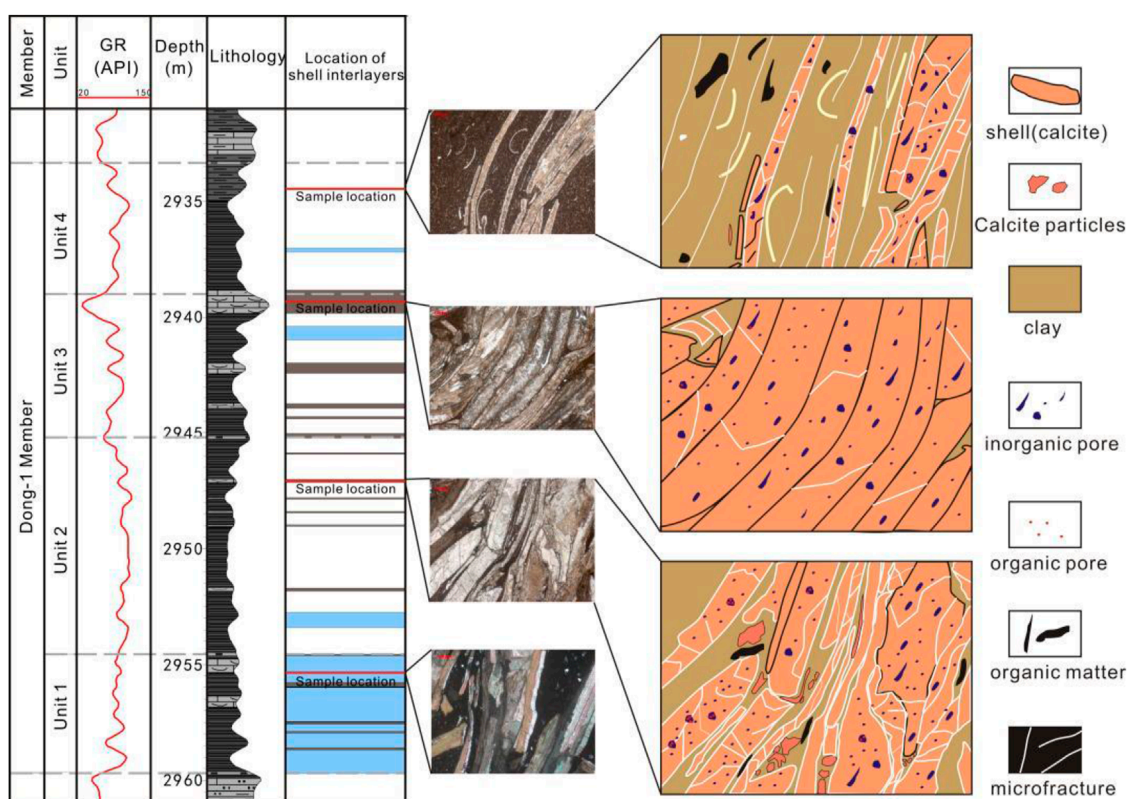


FIGURE 13
Schematic diagram of differential enrichment of organic matter in different types of shells in the Dong-1 member of Jurassic Ziliujing Formation, Fuxing area, East Sichuan Basin.

start of deposition of the Unit 4 sedimentary section, the climate turned warm and humid, and the lake expanded and deepened for an extended period. Increasing rainfall, biological production, and a slow deposition rate in the lake basin contributed to the deposition of a set of organic matter-rich shell-laminated shales.

Sedimentary model of the Dong-1 member

The sedimentary model of the Dong-1 shale is still unclear, and three sedimentary models have been proposed: (1) lake water periodic changes sedimentary model: shale deposits in a semi-deep to deep lake, and the shell interlayer deposits in the beach

shore facies of the shallow lake (He et al., 2022b); (2) storm event sedimentary model: shale deposited everywhere in the lake, while influenced by storm events, the shell fragments were brought from the shoal into the deep water, and the shell interlayer was deposited in the deep lake (Zhu et al., 2016); and (3) gravity flow sedimentary model: controlled by gravity flow, shells were transported from the shoal to the deep lake (Peng et al., 2022). The distribution of shells shows the normal and reverse rhythms, bottom scouring surfaces, and slump structures in Unit 1 that are typical of deepwater gravity flow sedimentary textures (Figure 7). In addition, the major and trace element concentrations indicate that the shale in Units 1–4 was deposited in a semi-deep lake with low oxygen levels. Peng et al. (2023) studied the Dong-1 shale in the Eastern Sichuan Basin and

found that the fine-grained sediments were deposited by gravity flows, which is consistent with the findings of this study.

The shell distribution in the Dong-1 shale is influenced by gravity flow in a shell-rich sub-lacustrine fan sedimentary depositional system (Walker, 1978) (Figure 8). Sedimentary lithofacies in the system can be classified into five microfacies. The first microfacies is the sedimentary channel, which exhibits a normal rhythm deposition of shell clasts. The shell clasts are broken at the bottom, whereas the upward transition to line-to-point contacts shows good stratification (Figure 9A). The second microfacies is the braided channel, which shows a normal rhythm deposition of shell clasts. The shell clasts are unbroken and make contact with each other at the bottom to form shell laminae. The upper part shows point contact and sporadic shells (Figure 9B). The third microfacies occurs in the depositional lobes and shows a reserve rhythm. Unbroken shell clasts at the bottom part have line-to-point contacts and show good stratification, whereas at the mid-to-upper part, the shell clasts are broken (Figure 9C). The fourth microfacies is thinly layered turbidites. In this microfacies, dispersed shells are laminated into mm-size laminae, and a small number of shell clasts are irregularly distributed in the black shale matrix (Figure 9D). The last microfacies is the down-cut channel sediments. The thickness of this microfacies ranges from 10 cm to 1 m with layered broken shell clasts. At the top of this microfacies, there is a sharp boundary between the shale matrix and limestone (Figure 9E).

The soft sediments are scoured by the wave action, forming a slump and convolution structure. The normal lacustrine wave action has a limited ability to transport sediments, whereas storm events have a stronger capability to scour and transport sediments. Storm events can trigger the large-scale movement of shell clasts from shallow water deposits to semi-deep to deep water through gravity flow. During sediment transportation, different-sized shell clasts are deposited sequentially and form a normal rhythm in the sedimentary channel and braided channel (Figures 8A,B, Figures 9A,B). However, long-distance transport deposits the shell clasts to the distal part and sub-lacustrine fan lobes with reverse rhythms (Figure 8C, Figure 9C). In addition, at the margin of the gravity flow, a small amount of shell mixed with black mud-sized sediments forms sporadic shell shale, which occurs mainly in the deepwater area of the inner fan region of the sub-lacustrine fan (Figure 8E, Figure 9E).

The Dong-1 member is deposited in an overall deepwater environment. The water depth from Units 1–3 oscillated periodically but decreased overall. The shell clast interlayers were, in general, deposited in a sub-lacustrine fan environment with a generally stable climate. However, the system experienced extreme climate changes during the deposition of the two thick shell interlayers. Rapid lake shrinkage led to a shallow water oxidizing environment and the deposition of shoal shell interlayers. The climate turned warm and humid in Unit 4, whereas rainfall increased the lake water depth and led to lake expansion and transgression (Figure 10).

Densification of shell layers

Although shell layers are composed of shell clasts, they show different petrophysical properties due to the effects of different processes. As the deposition of shell layers was closely related to

sedimentary environments, when volcano eruptions or gravity flow occurred, sedimentary environments and climate changed abruptly, resulting in a massive die-off of the bivalves. As a consequence, the thickness of the shell interlayer increased. In addition, the shell layers experienced multistage diagenesis processes that resulted in most of them forming tight (i.e., low porosity) intervals. At the start, there was significant breakage of the shells under compression during burial (Figure 3A), followed by the dissolution of the shell fragments and reprecipitation of calcite along the edges of the shells during petroleum generation. Subsequently, organic acids were generated, which dissolved the carbonate minerals, forming Ca^{2+} -rich fluids and clay minerals, releasing Fe, Mg, and Ca ions into the fluid. The ion saturation continued to increase, forming overpressure in the formation fluid and resulting in the rupture of the shell wall of the shell limestone and the formation of fibrous calcite (C3 and C6) that grew perpendicular to the joint surface. These diagenesis processes reduced interparticle pores and densified the shell layers. At the same time, the dissolution of shell clasts, precipitation of fibrous calcite along the shell edge, and cementation by ferrocalcite will also reduce porosity and densify the shell layer (Feng et al., 2023). Overall, the shell layers experienced the processes of densification–cementation, densification–accumulation, and preservation. As a result of these diagenesis processes, shell layers above and below the shale matrix become dense seal layers and restrict petroleum migration.

Influence of different shell layers on shale oil accumulation

Unlike other lacustrine shales, which contain siliceous and carbonate interlayers, the Dong-1 member is dominated by shell layers. During the deposition of the Dong-1 member, the water body in the area was fresh water, and freshwater bivalves were widely distributed across the Paleo-Asian continent. These freshwater bivalves favor warm and humid climates and are sensitive to the change in the environment (Cai, 1988; Deng et al., 2017). This type of carbonate bioclast varies in form, such as intact pieces and fragments, which originated from shallow-water shell beaches and were transported to semi-deep to deep water through gravity flow. The TOC concentrations of the shell interlayer are low (0.5%–1%) (Figure 2; Table 1), and SEM images show an absence of organic matter and only a small number of isolated intraparticle dissolution pores. These features indicate that shell interlayers may be sealing intervals, which have no petroleum generation potential and contribute very little to the total porosity. However, not all the shell interlayers are seals. A large number of dissolution pores and microfractures appear along the contact of shell layers and shale, and microfractures cut across the laminated shell and the layered shell interlayers and can provide storage space and migration pathways for petroleum (Figure 11). Consequently, these intervals are reservoirs rather than seal intervals.

As shown in Table 1, the shell-laminated clay-rich shale and shell-laminated clay-rich shale mainly occur in Units 2–4 and have the highest porosity (3.09%–5.42%). The shell rhythmic clay-rich shale has a higher porosity (2.21%) than the thickly layered shell interlayers (1.72%).

The SEM observations show that the shale is mainly in the form of organic pores and clay mineral intergranular pores (Figures 4A,B). In addition, a large number of dilation pores are found in the shell clasts, with pore size ranging from tens to hundreds of nanometers. Organic matter and organic matter pores also occur in the dilation pores (Figures 4C–F), providing additional storage space for petroleum. In the laminated shell layers in shale, the contact surface of the shell and shale is the weakest stress surface, and microfractures can form readily. Compression can fracture the shell clasts and generate microfractures (Figures 4C,D). The microfracture breadth can reach 7.37 μm (Figures 4A,B). In addition, microfractures can connect previously isolated pores and create pathways for petroleum migration (Figure 12). Shell interlayers and organic matter-rich shales are mixed in the layered shell interlayer. The shale matrix that overlays, underlies, and occurs within the shell interlayer, along with the shell interlayer itself, is classified as the second best source rock–reservoir combination (Figure 13). For the thick shell interlayer, shell clasts are compacted into densified tight layers, and no shale in-fill and no microfractures between shale clasts are observed through SEM. The amount of microfracturing within the shell clasts is less than that in the laminated shell and the layered shell interlayers. These sporadic microfractures cannot provide an efficient pathway for petroleum migration (Wang et al., 2021).

Conclusions

The Jurassic Dong-1 member in the Fuxing area is subdivided into four lithofacies. The shale of the four lithofacies is mainly developed with inorganic pores, but three types, namely, shell-laminated clay-rich shale, silt-shell-laminated clay-rich shale, and shell rhythmic clay-rich shale lithofacies, developed more microcracks, whereas the reservoir of shell limestone lithofacies is relatively dense, with little development of microcracks. The sub-lacustrine fan shell-rich shale of shale members was deposited in a semi-deep lake sedimentary environment under the influence of gravity flow. Three types of shales were deposited in a humid and warm climate in a strong reduced environment. On the one hand, the contact surface between the layers in the three rock phases and shale is prone to form microcracks under external forces, which is conducive to the storage and migration of oil and gas. On the other hand, the edges of the shell layers are easily dissolved by organic acids to form microcracks, which is conducive to the permeation of oil and gas. Therefore, the layer structure in shale is conducive to the enrichment of oil and gas. When the paleoclimate abruptly turned cold and dry, the water body became shallower and oxidizing, with higher salinity, and the mass die-off of freshwater bivalves occurred. The shell limestones were deposited in this environment and can only be sealed to prevent petroleum leakage and migration, not conducive to oil and gas enrichment.

Data availability statement

The raw data supporting the conclusions of this article will be made available by the authors, without undue reservation.

Author contributions

HB: conceptualization, funding acquisition, supervision, and writing – review and editing. YS: conceptualization, formal analysis, investigation, methodology, writing – original draft, and writing – review and editing. QW: formal analysis, investigation, writing – original draft, and writing – review and editing. YZ: conceptualization, funding acquisition, supervision, and writing – review and editing. MC: formal analysis, investigation, resources, and writing – review and editing. YL: formal analysis, investigation, supervision, and writing – review and editing. HL: funding acquisition, resources, and writing – review and editing. WP: funding acquisition, resources, and writing – review and editing.

Funding

The author(s) declare that financial support was received for the research and/or publication of this article. The study was funded by the research projects of SINOPEC (No. P23077 and No. P21078-2) and Fundamental Research Funds for the Central Universities, the China University of Petroleum (East China) (No. 23CX06003A). The authors declare that this study received funding from SINOPEC. The funder was not involved in the study design, collection, analysis, interpretation of data, the writing of this article, or the decision to submit it for publication.

Acknowledgments

The authors appreciate the core and data access assistant provided by the team members of the Jiangnan Oilfield Branch Company, Sinopec, for their basic exploration work.

Conflict of interest

Authors HB, YS, YZ, MC, HL, and WP were employed by Jiangnan Oilfield Branch Company.

The remaining authors declare that the research was conducted in the absence of any commercial or financial relationships that could be construed as a potential conflict of interest.

Generative AI statement

The author(s) declare that no Generative AI was used in the creation of this manuscript.

Publisher's note

All claims expressed in this article are solely those of the authors and do not necessarily represent those of their affiliated organizations, or those of the publisher, the editors and the reviewers. Any product that may be evaluated in this article, or claim that may be made by its manufacturer, is not guaranteed or endorsed by the publisher.

References

- Algeo, T. J., Marenco, P. J., and Saltzman, M. R. (2016). Coevolution of oceans, climate, and the biosphere during the "Ordovician Revolution": a review. *Palaeogeogr. Palaeoclimatol. Palaeoecol.* 458, 1–11. doi:10.1016/j.palaeo.2016.05.015
- Alnahwi, A., Loucks, R. G., Ruppel, S. C., Scott, R. W., and Tribouillard, N. (2018). Dip-related changes in stratigraphic architecture and associated sedimentological and geochemical variability in the Upper Cretaceous Eagle Ford Group in south Texas. *AAPG Bull.* 102, 2537–2568. doi:10.1306/05111817310
- Bai, Y., Liu, Z., Sun, P., Liu, R., Hu, X., Zhao, H., et al. (2015). Rare earth and major element geochemistry of Eocene fine-grained sediments in oil shale and coal-bearing layers of the Meihe Basin, Northeast China. *J. Asian Earth Sci.* 97, 89–101. doi:10.1016/j.jseas.2014.10.008
- Bechtel, A., Oberauer, K., Kostić, A., Gratzner, R., Milisavljević, V., Aleksić, N., et al. (2018). Depositional environment and hydrocarbon source potential of the Lower Miocene oil shale deposit in the Aleksinac Basin (Serbia). *Org. Geochem.* 115, 93–112. doi:10.1016/j.orggeochem.2017.10.009
- Bohacs, K. M., Carroll, A. R., and Neal, J. E. (2000). Lake-basin type, source potential, and hydrocarbon character: an integrated sequence-stratigraphic geochemical framework (in lake basins through space and time). *AAPG Bull.* 83, 143–162. doi:10.1306/St46706C1
- Cai, S. (1988). Fresh water bivalve fossils in the jurassic zhiliujing formation, chongqing and hechuan area, sichuan. *Prof. Pap. Stratigr. Paleontology* 21, 128–150. Available online at: https://kns.cnki.net/kcms2/article/abstract?v=gHWJqxSIt2QFGL_Q40dCBAUoKWbeW3ipvx6nkGSPqs-1cVTvm0s_HE6fn1-o-eVCwWmsjK9mAO0bHUGi64MWSBikNvva23BJJKP4hBWIrA7tp--pMTiU3ekesyMwgfvXgQ6OaRw67s69hS1-VcDeknn_gVVJNEKkVkgFFHQ_pvuNxHZTqQ==&uniplatform=NZKPT&language=CHS (Accessed June 27, 2025).
- Calvert, S. E., and Pedersen, T. F. (1993). Geochemistry of recent oxic and anoxic marine sediments: implications for the geological record. *Mar. Geol.* 113 (1–2), 67–88. doi:10.1016/0025-3227(93)90150-t
- Chalmers, G. R., Bustin, R. M., and Power, I. M. (2012). Characterization of gas shale pore systems by porosimetry, pycnometry, surface area, and field emission scanning electron microscopy/transmission electron microscopy image analyses: examples from the Barnett, Woodford, Haynesville, Marcellus, and Doig units. *AAPG Bull.* 96, 1099–1119. doi:10.1306/10171111052
- Chamberlain, C. P., Wan, X., Graham, S. A., Carroll, A. R., Doebbert, A. C., Sageman, B. B., et al. (2013). Stable isotopic evidence for climate and basin evolution of the late cretaceous Songliao Basin, China. *Palaeogeogr. Palaeoclimatol. Palaeoecol.* 385 (3), 106–124. doi:10.1016/j.palaeo.2012.03.020
- Chen, C., Mu, C., Zhou, K., Liang, W., Ge, X., Wang, X., et al. (2016). The geochemical characteristics and factors controlling the organic matter accumulation of the Late Ordovician-Early Silurian black shale in the Upper Yangtze Basin, South China. *Mar. Petroleum Geol.* 76, 159–175. doi:10.1016/j.marpetgeo.2016.04.022
- Chen, D., Wang, J., Yan, D., Wei, H., Yu, H., and Wang, Q. (2011). Environmental dynamic of organic accumulation for the principal Paleozoic source rock on Yangtze block. *Geol. Sci.* 46 (1), 5–26. Available online at: http://www.dzcx.org/data/article/geology/preview/pdf/geology_8479.pdf (Accessed June 27, 2025).
- Chen, J., Deng, X., Li, S., Chu, M., Li, S., Qiu, J., et al. (2023). Oil-source correlation and secondary migration paths in the triassic chang 10 of the yanchang Formation in the zhidan area, Ordos Basin, China: evidence from biomarkers, rare earth elements, and carbazole signatures. *Nat. Resour. Res.* 32, 1683–1710. doi:10.1007/s11053-023-10203-6
- Dean, W. E., Gardner, J. V., and Piper, D. Z. (1997). Inorganic geochemical indicators of glacial interglacial changes in productivity and anoxia on the California continental margin. *Geochimica Cosmochimica Acta* 61 (21), 4507–4518. doi:10.1016/s0016-7037(97)00237-8
- Deng, S., Lu, Y., Zhao, Y., Ru, F., Wang, Y., Yang, X., et al. (2017). The Jurassic paleoclimate regionalization and evolution of China. *Earth Sci. Front.* 24 (1), 106–142.
- Desborough, G. A. (1978). A biogenic-chemical stratified lake model for the origin of oil shale of the Green River Formation: an alternative to the playa-lake model. *Geol. Soc. Am. Bull.* 89, 961–971. doi:10.1130/0016-7606(1978)89<961:abslmf>2.0.co;2
- Ding, X., Liu, G., Zha, M., Gao, C., Huang, Z., Qu, J., et al. (2016). Geochemical characterization and depositional environment of source rocks of small fault basin in Erlian Basin, northern China. *Mar. Petroleum Geol.* 69, 231–240. doi:10.1016/j.marpetgeo.2015.11.006
- Doebbert, A. C., Carroll, A. R., Mulch, A., Chetel, L. M., and Chamberlain, C. P. (2010). Geomorphic controls on lacustrine isotopic compositions: evidence from the lancy member, green river formation, Wyoming. *Geol. Soc. Am. Bull.* 122, 236–252. doi:10.1130/b26522.1
- Feng, M., Luo, Z., Liu, X., Zhu, H., Zeng, D., and Wang, X. (2023). Model of Calcite precipitation in a shell limestone interlayer and densification of the Dongyuemiao Reservoir (Lower Jurassic) in the Northern Sichuan Basine. *Acta Petrol. Sin.* 32, 1–16.
- Feng, Z., Fang, W., Li, Z., Wang, X., Huo, Q., Huang, C., et al. (2011). Depositional environment of terrestrial petroleum source rocks and geochemical indicators in the Songliao Basin. *Sci. China Earth Sci.* 54, 1304–1317. doi:10.1007/s11430-011-4268-0
- Hatch, J. R., Jacobson, S. R., Witzke, B. J., Risatti, J. B., Anders, D. E., Watney, W. L., et al. (1987). Possible late middle ordovician organic carbon isotope excursion: evidence from ordovician oils and hydrocarbon source rocks, mid-continent and east-central United States. *AAPG Bulletin* 71 (11), 1342–1354.
- He, J., Cheng, Z., Dong, D., Sun, S., and Wang, Z. (2022a). The evolution of sedimentary environments of Dongyuemiao Member and key factors for enrichment of shale oil and gas, northeastern Sichuan Basin. *Sediment. Geol. Tethyan Geol.* 42 (3), 385–397.
- He, L., Wang, Y. P., and Chen, D. F. (2021). Organic carbon and nitrogen isotope anomalies during the late Ordovician in Sichuan Basin, and implications for paleoenvironment. *Geochimica* 50 (6), 623–634.
- He, W., Meng, Q., Fu, X., Zheng, Q., Su, Y., and Cui, K. (2022b). Sedimentary environment characteristics and organic matter enrichment mechanism of Qingshankou Formation shale in Gulong Sag, Songliao Basin. *J. Sedimentology*, 1–21.
- Hu, D., Shu, Z., Guo, Z., Li, X., and Chen, M. (2021). Discovery of China's first shale condensate gas reservoir in the jurassic system (FY10HF well) in the fuxing area of East Sichuan. *Geol. China* 48 (06), 1980–1981.
- Hua, G., Wu, S., Qiu, Z., Jing, Z., Xu, J., and Guan, M. (2020). Laminae texture and its effect on reservoir properties: a case study of Longmaxi Shale, Sichuan Basin. *Acta Sedimentol. Sin.* 110, 1–22.
- Hua, G., Wu, S., Zhang, J., Liu, R., Guan, M., Cai, Y., et al. (2022). Laminar structure and reservoir quality of shales with high clay mineral content in the Qingshankou Formation, Songliao Basin. *Energies* 15 (2), 6132. doi:10.3390/en15176132
- Huang, Z., Liu, G., Li, T., Li, Y., Yin, Y., and Wang, L. (2017). Characterization and control of mesopore structural heterogeneity for low thermal maturity shale: a case study of Yanchang formation shale, ordos basin. *Energy and Fuels* 31 (11), 11569–11586. doi:10.1021/acs.energyfuels.7b01414
- Jarvie, D. M., Hill, R. J., Ruble, T. E., and Pollastro, R. M. (2007). Unconventional shale-gas systems: the Mississippian Barnett Shale of north-central Texas as one model for thermogenic shale-gas assessment. *AAPG Bull.* 91 (4), 475–499. doi:10.1306/12190606068
- Jia, C., Zou, C., Li, J., Li, D., and Zheng, M. (2012). Assessment criteria, main types, basic features and resources prospects of the tight oil in China. *Acta Petrolei Sinica* 33 (3), 343–350.
- Jia, J., Liu, Z., Bechtel, A., Strobl, S. A. I., and Sun, P. (2013). Tectonic and climate control of oil shale deposition in the upper cretaceous Qingshankou formation (Songliao Basin, NE China). *Int. J. Earth Sci.* 102, 1717–1734. doi:10.1007/s00531-013-0903-7
- Jin, Z., Wang, G., Liu, G., Gai, B., Liu, Q., Wang, H., et al. (2021). Research progress and key scientific issues of continental shale oil in China. *J. Petroleum* 42 (7), 821–835.
- Katz, B. J. (1995). Factors controlling the development of lacustrine petroleum source rocks—An update. In: *Paleogeography, paleoclimate, and source rocks*. Tulsa: American Association of Petroleum Geologists, 61–79.
- Lamotte, F. D., Fourdan, B., Leleu, S., Leparmentier, F., and Clarens, P. D. (2015). Style of rifting and the stages of Pangea breakup. *Tectonics* 34 (5), 1009–1029. doi:10.1002/2014tc003760
- Langmann, B., Zákšek, K., Hort, M., and Duggen, S. (2010). Volcanic ash as fertilizer for the surface ocean[J]. *Atmos. Chem. Phys.*, 10, 8, 3891–3899. doi:10.5194/acp-10-3891-2010
- Li, J. J., Wang, W. M., Cao, Q., Shi, Y. L., Yan, X. T., and Tian, S. S. (2015). Impact of hydrocarbon expulsion efficiency of continental shale upon shale oil accumulations in eastern China. *Mar. Petroleum Geol.* 59, 467–479. doi:10.1016/j.marpetgeo.2014.10.002
- Li, M., Jin, Z., and Dong, M. (2020). Advances in the basic study of lacustrine shale evolution and shale oil accumulation. *Petroleum Geol. and Exp.* 48 (4), 408–505.
- Liang, C., Cao, Y., Jiang, Z., Wu, J., Guoqi, S., and Wang, Y. (2017). Shale oil potential of lacustrine black shale in the Eocene Dongying depression: implications for geochemistry and reservoir characteristics. *AAPG Bull.* 101 (11), 1835–1858. doi:10.1306/01251715249
- Lin, Z., Chen, D., and Liu, Q. (2008). Geochemical indices for redox conditions of marine sediments. *Bull. Mineralogy, Petrology Geochem.* 27 (1), 72–80.
- Lindström, S., Callegarob, S., Davies, J., Tegner, C., Bas, V., Pedersen, G., et al. (2021). Tracing volcanic emissions from the central Atlantic magmatic province in the sedimentary record. *Earth-Science Rev.* 212, 103444. doi:10.1016/j.earscirev.2020.103444
- Lindström, S., Sanei, H., Schootbrugge, B., Pedersen, G., Outridge, P., Tegner, C., et al. (2019). Volcanic mercury and mutagenesis in land plants during the end-Triassic mass extinction. *Sci. Adv.* 5 (10), aaw4018. doi:10.1126/sciadv.aaw4018
- Liu, A., Chen, L., Chen, X., Tian, W., Li, H., Qie, W., et al. (2021). Carbon and oxygen isotope characteristics of Devonian in central Hunan depression and its paleoenvironmental significance. *J. Earth Sci.* 46 (4), 1269–1280 in Chinese. doi:10.3799/dqkx.2020.362

Liu, B., Shi, J., and Fu, X. (2018). Petrological characteristics and shale oil enrichment of lacustrine fine-grained sedimentary system: a case study of organic-rich shale in first member of Cretaceous. *Petroleum Explor. Dev.* 45 (5), 1–11.

Liu, Y., Li, C., Algeo, T. J., Fan, J., and Peng, P. (2016). Global and regional controls on marine redox changes across the Ordovician-Silurian boundary in South China. *Palaeogeogr. Palaeoclimatol. Palaeoecol.* 463, 180–191. doi:10.1016/j.palaeo.2016.10.006

Lu, Y., Jiang, S., Lu, Y., Xu, S., Shu, Y., and Wang, Y. (2019). Productivity or preservation? The factors controlling the organic matter accumulation in the late Katian through Hirnantian Wufeng organic-rich shale, South China. *Mar. Petroleum Geol.* 109, 22–35. doi:10.1016/j.marpetgeo.2019.06.007

Ma, Y., Du, X., Liu, H., and Lu, Y. (2017). Characteristics, depositional processes, and evolution of shale lithofacies of the upper submember of E2s4 in the Dongying Depression. *Earth Sci.* 42 (7), 1195–1208.

Marco, F., Jin, X., Shi, Z., Chen, B., Preto, N., et al. (2022). High-resolution record of multiple organic carbon-isotope excursions in lacustrine deposits of upper sinemurian through pliensbachian (early jurassic) from the Sichuan Basin, China. *GSA Bulletin* 135 (1-2), 3–17. doi:10.1130/B36235.1

Marisa, S. S., Stephen, P. H., Hugh, C. J., Micha, R., Clemens, V. U., Wei, M. X., et al. (2020). Orbital pacing and secular evolution of the Early Jurassic carbon cycle. *Proc. Natl. Acad. Sci. U. S. A.* 117, 3974–3982.

McLennan, S. M. (1993). Weathering and global denudation. *J. Geol.* 101 (2), 295–303. doi:10.1086/648222

Meng, Q., and Zhang, G. (1999). Timing of collision of the north and south China blocks: controversy and reconciliation. *Geology* 27, 123–126. doi:10.1130/0091-7613(1999)027<0123:tocotn>2.3.co;2

Milliken, K. L. (2003). Diagenesis. In: G. V. Middleton, editor. *Encyclopedia of sediments and sedimentary rocks*. Dordrecht, Boston: London Kluwer Academic Publishers. p. 214–219.

Nesbitt, H. W., and Young, G. M. (1989). Formation and diagenesis of weathering profiles. *J. Geol.* 97 (2), 129–147. doi:10.1086/629290

Nesbitt, H. W., Young, G. M., McLennan, S. M., and Keays, R. R. (1996). Effects of chemical weathering and sorting on the petrogenesis of siliciclastic sediments, with implications for provenance studies. *J. Geol.* 104 (5), 525–542. doi:10.1086/629850

Peng, J., Liu, Z., Feng, D., and Wang, Q. (2022). Sedimentology and sequence stratigraphy of lacustrine deep-water fine-grained sedimentary rocks: the lower jurassic Dongyuemiao Formation in the Sichuan Basin, Western China. *Mar. Petroleum Geol.* 146, 105933. doi:10.1016/j.marpetgeo.2022.105933

Peng, J., Liu, Z., Feng, D., and Wang, Q. (2023). Variations of organic matter content and type within the sequence stratigraphic framework of the lacustrine deep-water Dongyuemiao formation, Sichuan Basin, Western China. *Mar. Petroleum Geol.* 149, 106104. doi:10.1016/j.marpetgeo.2023.106104

Qiu, Z., and He, J. (2021). Depositional environment changes and organic matter accumulation of Pliensbachian-Toarcian lacustrine shales in the Sichuan basin, SW China. *J. Asian Earth Sci.* 232, 105035. doi:10.1016/j.jseae.2021.105035

Schenau, S. J., Prins, M. A., De Lange, G. J., and Monnin, C. (2001). Barium accumulation in the Arabian Sea: controls on barite preservation in marine sediments. *Geochem. Cosmochimica Acta* 65 (10), 1545–1556. doi:10.1016/s0016-7037(01)00547-6

Schöllhorn, I., Adatte, T., Charbonnier, G., Mattioli, E., Spangenberg, J. E., and Foellmi, K. B. (2020). Pliensbachian environmental perturbations and their potential link with volcanic activity: Swiss and British geochemical records. *Sediment. Geol.* 406, 105665. doi:10.1016/j.sedgeo.2020.105665

Shi, Y., Jin, Z., Liu, Q., Zhang, T., Fan, T., and Gao, Z. (2022). Laminar characteristics of lacustrine organic-rich shales and their significance for shale reservoir formation: a case study of the Paleogene shales in the Dongying Sag, Bohai Bay Basin, China. *J. Asian Earth Sci.* 223, 104976. doi:10.1016/j.jseae.2021.104976

Shu, Y., Bao, H., Zheng, Y., Chen, M., Lu, Y., Liu, H., et al. (2021). Lithofacies types, assemblage characteristics and sedimentary evolution model of lacustrine shale in Dongyuemiao formation of Fuxing area. *Front. Earth Sci.* 9, 1034. doi:10.3389/feart.2021.772581

Thomson, J., Jarvis, I., Green, D. R. H., and Green, D. (1998). Oxidation fronts in Madeira Abyssal Plain turbidites: Persistence of early diagenetic trace-element enrichments during burial, Site 950. *Proc. Ocean Drill. Program, Sci. Results* 157, 559–571.

Tribouillard, N., Algeo, T. J., Lyons, T., and Ribouilleau, A. (2006). Trace metals as paleoredox and paleoproductivity proxies: an update. *Chem. Geol.* 232 (1-2), 12–32. doi:10.1016/j.chemgeo.2006.02.012

Walker, R. G. (1978). Deep-water sandstone facies and ancient submarine fans: models for exploration for stratigraphic traps. *AAPG Bull.* 62 (6), 932–966. doi:10.1306/c1ea4f77-16c9-11d7-8645000102c1865d

Wang, Q., Hu, Q., Larsen, C., Zhao, C., Sun, M., Zhang, Y., et al. (2021). Microfracture-pore structure characterization and water-rock interaction in three lithofacies of the Lower Eagle Ford Formation. *Eng. Geol.* 292, 106276. doi:10.1016/j.enggeo.2021.106276

Wang, Q., Hu, Q., Zhao, C., Yang, X., Zhang, T., Ilavsky, J., et al. (2022). Micro to nano-scale areal heterogeneity in pore structure and mineral compositions of a sub-decimeter-sized Eagle Ford Shale. *Int. J. Coal Geol.* 261, 104093. doi:10.1016/j.coal.2022.104093

Wang, Y., Xu, S., Hao, F., Lu, Y., Shu, Z., Yan, D., et al. (2019). Geochemical and petrographic characteristics of Wufeng-Longmaxi shales, Jiaoshiba area, southwest China: implications for organic matter differential accumulation. *Mar. Petroleum Geol.* 102, 138–154. doi:10.1016/j.marpetgeo.2018.12.038

Wan Hsiaiah, A., Lee, C. P., Gou, P., Shuib, M. K., Ng, T. F., Albaghdady, A. A., et al. (2012). Coal-bearing strata of Labuan: mode of occurrences, organic petrographic characteristics and stratigraphic associations. *J. Asian Earth Sci.* 76, 334–345. doi:10.1016/j.jseae.2013.05.017

Wei, W., and Algeo, T. J. (2019). Elemental proxies for paleosalinity analysis of ancient shales and mudrocks. *Geochem. Cosmochimica Acta* 287, 341–366. doi:10.1016/j.gca.2019.06.034

Wei, W., Algeo, T. J., Lu, Y., Lu, Y., Liu, H., Zhang, S., et al. (2018). Identifying marine incursions into the Paleogene Bohai Bay Basin lake system in northeastern China. *Int. J. Coal Geol.* 200, 1–17. doi:10.1016/j.coal.2018.10.001

Wu, L., Lu, Y., Jiang, S., Liu, X., Liu, Z., and Lu, Y. (2019). Relationship between the origin of organic-rich shale and geological events of the Upper Ordovician-Lower Silurian in the Upper Yangtze area. *Mar. Petroleum Geol.* 102, 74–85. doi:10.1016/j.marpetgeo.2018.11.017

Xu, Q., Liu, B., Ma, Y., Song, M., Wang, Y., and Chen, Z. (2017). Geological and geochemical characterization of lacustrine shale: a case study of the Jurassic Daanzhai member shale in the Central Sichuan Basin, Southwest China. *J. Nat. Gas Sci. Eng.* 47, 124–139. doi:10.1016/j.jngse.2017.09.008

Zhang, S., Liu, H. M., Chen, S. Y., Wang, Y., Pu, X., Zhang, K., et al. (2017). Classification scheme for lithofacies of fine-grained sedimentary rocks in faulted basins of eastern China: insights from the fine-grained sedimentary rocks in Paleogene, southern Bohai Bay Basin. *Acta Geol. Sin.* 91 (5), 1108–1119.

Zhang, S., Wei, C., Zhao, Z., and Jie, S. (1996). Formation and metamorphic evolution of the Douling complex from the East Qinling mountains. *Sci. China Earth Sci.* 39, 80–86.

Zhang, S., Zhang, B., Bian, L. J. Z., Wang, D., Zhang, X., Gao, Z., et al. (2005). Development constraints of marine source rocks in China. *Geol. Sci.* 12 (3), 39–48.

Zhang, X., Lv, P. Z., Fang, L. H., Yang, H., Deng, S. Z., Lu, Y. Z., et al. (2022b). Wildfire records across the Triassic-Jurassic boundary in the Southern Margin of the Junggar Basin, and global correlations. *Acta Sedimentol. Sin.* 40 (2), 473–483.

Zhang, X., Yang, H., Ren, J. H., Fang, L. H., Wu, t., Miao, Y. F., et al. (2022a). Palynological assemblages and palaeoclimate across the Triassic-Jurassic boundary in the Haojiagou section, southern Junggar Basin. *Chinese Journal of Geology* 57 (04), 1161–1176.

Zhou, Y. Q., Chai, Z. F., Xu, Y. T., and Peng, H. (1995). Methodology for the Determination of Magnesium Isotope Composition in Geological Samples with an Ion Mass Spectrometer. *Rock Mineral Analysis* 14 (01), 7–14.

Zhu, T., Long, S. X., Wang, F., and Peng, Y. M. (2016). Sedimentary patterns and lithofacies types of lacustrine shale in the Sichuan Basin. *Nat. Gas. Ind.* 36 (08), 22–28.

Zou, C., Yang, Z., Zhu, R., Wu, S., Fu, J., Lei, D., et al. (2019). Geologic significance and optimization technique of sweet spots in unconventional shale systems. *J. Asian Earth Sci.* 178, 3–19. doi:10.1016/j.jseae.2018.07.005